Journal of Atmospheric Chemistry **26:** 223–274, 1997.

© 1997 *Kluwer Academic Publishers. Printed in the Netherlands.*

Tropospheric Ozone in a Global-Scale Three-Dimensional Lagrangian Model and Its Response to NO_X Emission Controls

W. J. COLLINS, D. S. STEVENSON, C. E. JOHNSON and R. G. DERWENT
Meteorological Office, Bracknell, Berkshire RG12 2SZ, United Kingdom

(Received: 21 September 1995; in final form: 29 January 1997)

Abstract. A three-dimensional Lagrangian tropospheric chemistry model is used to investigate the impact of human activities on the tropospheric distribution of ozone and hydroxyl radicals. The model describes the behaviour of 50 species including methane, carbon monoxide, oxides of nitrogen, sulphur dioxide and nine organic compounds emitted from human activities and a range of other sources. The chemical mechanism involves about 100 chemical reactions of which 16 are photochemical reactions whose diurnal dependence is treated in full. The model utilises a five minute chemistry time step and a three hour advection time step for the 50,000 air parcels. Meteorological data for the winds, temperatures, clouds and so on are taken from the UK Meteorological Office global model for 1994 onwards. The impacts of a 50% reduction in European NO_X emissions on global ozone concentrations are assessed. Surface ozone concentrations decrease in summertime and rise in wintertime, but to different extents.

Key words: global model, three-dimensional, Lagrangian tropospheric chemistry, ozone, NO_X, emission controls.

1. Introduction

Over the past few decades, understanding of the behaviour of ozone in the troposphere has changed considerably. Originally, tropospheric ozone was seen as largely controlled by the stratosphere aloft and by destruction at the Earth's surface. The formation of photochemical smog in the Los Angeles basin was thought to be a rather localised phenomenon. Levy (1971) drew attention to the importance of the photolysis of tropospheric ozone as a driving mechanism for the chemistry of hydroxyl (OH) and hydroperoxy (HO_2) free radicals linking together the life cycles of methane, carbon monoxide, oxides of nitrogen and ozone. Crutzen (1974) pointed out that tropospheric photochemical production and destruction of ozone were in approximate balance, with stratospheric input and surface removal of similar but smaller magnitudes.

Human activities can influence the tropospheric distribution of ozone through a number of mechanisms in addition to the formation of Los Angeles smog in the urban boundary layer (Haagen-Smit *et al.*, 1953). They have influenced the emissions of the major tropospheric source gases: methane (Rasmussen and Khalil,

1986; Blake and Rowland, 1986), carbon monoxide (Cicerone, 1988), oxides of nitrogen (Crutzen and Gidel, 1983; Logan, 1985) and hydrocarbons (Hough and Derwent, 1990) which control the tropospheric distribution of hydroxyl radicals and hence ozone production and destruction.

Observational evidence for an increase in tropospheric ozone since preindustrial times has been reviewed elsewhere (IPCC, 1995; WMO, 1995). Levels are likely to have doubled in the Northern Hemisphere since preindustrial times (Volz and Kley, 1988). Models of the influence of human activities on the coupled life cycles of the tropospheric source gases have shown that they may indeed have caused this observed increase (Hough and Derwent, 1990). Increased levels of ozone can cause damage to human health and the natural environment (WHO, 1987).

It has been pointed out that modelling tropospheric ozone is a difficult task because of the large number of processes involved (IPCC, 1995). Understanding of the emissions of the tropospheric source gases and chemical mechanisms is rudimentary. The key ozone precursor gases are not well-mixed and their impact on the tropospheric ozone life cycle is likely to be spatially variable and inhomogeneous. Most of the models used to study the influence of human activities on tropospheric ozone have been two-dimensional (altitude-latitude) and their relative performances have been evaluated in IPCC (1995) and WMO (1995). These have been shown to be inadequate to model ozone correctly (Kanakidou and Crutzen, 1993). Three-dimensional (altitude, latitude and longitude) studies have started to appear (Penner *et al.*, 1991; Kasibhatla *et al.*, 1993; Jacob *et al.*, 1993; Lelieveld and Crutzen, 1994) addressing tropospheric ozone. In this paper we extend these three-dimensional studies of the role of NO_X and ozone chemistry including a large range of hydrocarbons and looking at the impact of regional scale NO_X emission reductions on tropospheric ozone.

2. The Global 3-D Chemistry Transport Model

There is a strong case for extending our previous tropospheric ozone modelling from a low resolution two-dimensional model to three-dimensions and so to improve considerably the spatial resolution of the hydrocarbons and NO_X chemistry. So far the main approach to three-dimensional tropospheric chemistry modelling has been Eulerian. In this approach a regular rectangular grid is built throughout the model domain and a finite-differencing scheme is used to describe the processes involved in this fixed framework. The accurate representation of the advection of trace gases is not straightforward if negative concentrations, numerical dispersion and short timesteps are to be avoided (Chock and Winkler, 1994; Dabdub and Seinfeld, 1994). Pseudospectral techniques offer a formally accurate alternative to the conventional finite difference approach in models of atmospheric dynamics. However, when applied to atmospheric trace gas transport, they may generate negative concentrations and spurious oscillations.

Table I. Table of chemical species used in the model

$O(^1D)$	C_2H_4	$CH_3COCOCH_3$
$O(^3P)$	C_3H_6	methyl maleic dialdehyde
O_3	o-xylene	$CHOCH(OH)CO_2CH_3CHO$
OH	toluene	methyl vinyl ketone
HO_2	isoprene	glyoxal
NO	H_2O_2	methyl-glyoxal
NO_2	CH_3COOH	$HOC_6H_4(CH_3)_2O_2$
NO_3	HCHO	$HOC_6H_5CH_3O_2$
N_2O_5	CH_3CHO	$HOC_5H_8O_2$
HNO_3	CH_3O_2	$CH_3COCH(O_2)CH_2OH$
peroxy acetyl nitrate	$C_2H_5O_2$	$NO_3C_2H_4O_2$
H_2	sec-$C_4H_9O_2$	$NO_3C_3H_6O_2$
H_2O_2	CH_3COO_2	$NO_3C_5H_8O_3$
CO	$CH_3COC_2H_5$	$NO_3C_6H_4(CH_3)_2O_2$
CH_4	$CH_3COCHO_2CH_3$	nitrate aerosol
C_2H_6	$CH_3CHO_2CH_2OH$	SO_2
n-C_4H_{10}	$CH_2O_2CH_2OH$	sulphate aerosol

In this study a Lagrangian approach has been adopted using 50 000 constant mass parcels of air, the centroids of which are advected by interpolated winds from the United Kingdom Meteorological Office UM global circulation model (Cullen, 1993). By this method, all trace gas species are advected together so the chemistry and transport processes can be uncoupled and chemistry timesteps determined locally. There are disadvantages with the Lagrangian approach; species concentrations are defined on parcel centroids but output is generally required on an Eulerian grid and this may be over- or underdetermined in a practical implementation where the number of parcels may be limited and distortions due to wind shears can render the notion of a distinct air parcel meaningless.

Our implementation of the Lagrangian approach to three-dimensional chemistry and transport differs in a number of respects from the GRANTOUR model (Walton *et al.*, 1988; Penner *et al.*, 1991) including the handling of diffusion, reinitialisation of particles and the handling of emissions and deposition. The chemical scheme adopted is based on that used with considerable success in developing European regional scale pollution control policies for ozone within the United Nations Economic Commission for Europe EMEP programme (Eliassen *et al.*, 1982; Simpson, 1991, 1992a). A list of species is shown in Table I.

Table II. Table of the coefficient A used in model to calculate the hybrid height coordinate η, and the pressures and approximate heights of the layers used for the model output. The coefficient A is based on that used in the Meteorological Office Unified Model GCM. The mean pressure is appropriate for the oceans with mean sea level pressure of 1013 hPa, for η close to 1.0 the pressure will be significantly less over high ground. The approximate height is based on a surface pressure of 1013 hPa and a temperature profile taken from the U.S. Standard Atmosphere (1976). Close to the ground the height corresponds to the height above the ground, but at the smaller η values corresponds to the height above the 1000 hPa surface

Model output level	η	A (hPa)	Mean pressure (hPa)	Approximate height (km)
1	1.0–0.9	0.0–0.0	1013–912	0.0–1.0
2	0.9–0.8	0.0–4.2	912–810	1.0–2.0
3	0.8–0.7	4.2–24.0	810–709	2.0–3.0
4	0.7–0.6	24.0–57.9	709–607	3.0–4.2
5	0.6–0.5	57.9–96.3	607–505	4.2–5.6
6	0.5–0.4	96.3–128.8	505–404	5.6–7.2
7	0.4–0.3	128.8–146.9	404–302	7.2–9.2
8	0.3–0.2	146.9–136.7	302–201	9.2–11.8
9	0.2–0.1	136.7–89.1	201–100	11.8–16.2

2.1. ADVECTION SCHEME

The height coordinate in the Meteorological Office Unified Model is a hybrid η coordinate. This is derived from the atmospheric pressure at that height and the atmospheric pressure at the surface by the relation:

$$\eta = \frac{P}{P_s} + A\left(\frac{1}{P_0} - \frac{1}{P_s}\right) , \tag{1}$$

where P is the pressure, P_s is the surface pressure, P_0 is a reference pressure (= 1000 hPa) and A is a coefficient having the dimensions of pressure. Values of A are listed in Table II. A is equal to zero near the surface and is equal to the pressure for heights greater than 30 hPa. Near the surface η is terrain-following and is equal to P/P_s, above a height of 30 hPa η follows the pressure surfaces and is equal to P/(1000 hPa).

The Lagrangian cells are advected according to winds taken from the Meteorological Office Unified Model archive, which are based on a grid of 1.25° longitude, 0.8333° latitude and 9 unevenly-spaced η levels between 0.997 and 0.0992 for the horizontal winds (v_U and v_V) and between 0.952 and 0.075 for the vertical wind (v_W).

The winds are stored on the archive every six hours which is more data than the program can handle, so every 18 days the 18 day means and standard deviations are calculated for each wind component at each grid point. The period of 18 days was chosen as it is the largest that can be read off the archive at once.

The mean and standard deviation winds for a particular Lagrangian cell are calculated from the cell position using a three-dimensional tri-linear interpolation. The wind components are then determined using the mean and a random fraction of the standard deviation.

$$v_i = \bar{v_i} + S_i\sigma_i + \tfrac{1}{2}\nabla_i\sigma_i^2 \; ; \; i = U, V \text{ or } W, \tag{2}$$

where $\bar{v_i}$ is the mean wind component, σ_i is the standard deviation of the wind component, S_i is a normally-distributed random number and ∇_i is the i component of the gradient operator. The last term is a drift correction which takes into account the effect that the cell will tend to drift in the direction of increasing variance (Thomson, 1987). The advection timestep is typically set to three hours so within that time some cells may traverse more than one meteorological grid square and so follow an incorrect trajectory, we have compared the effects of using smaller timesteps with radon as a tracer (Stevenson *et al.*, 1997b) and found no noticeable difference to the modelled radon distribution.

2.1.1. *Convection*

Small-scale convective processes (i.e. smaller than can be resolved on the gridded wind data) can have a large influence on the tropospheric chemistry by lifting pollutants out of the boundary layer or bringing down O_3 and NO from the top of the troposphere (Ehhalt *et al.*, 1992). We have included convection in our model using convective cloud fields diagnosed by the Unified Model (these include convective cloud top height, convective cloud cover and convective precipitation). We mix completely a fraction of the cells throughout the column below the cloud top. The fraction mixed is given by by the amount of cloud cover for clouds that are not precipitating, or by a mass flux calculated from the precipitation rate for those that are precipitating using a formula taken from Chatfield and Delany (1990). The mass flux is converted to a fraction by dividing it by the mass of air beneath the cloud base. The effect of convection on a tracer was compared with the U.K. Met. Office Unified Model (UM) GCM using radon as a short lived tracer. Our model was found to transport species in a manner very similar to the UM.

2.1.2. *Inter-Parcel Exchange*

During the advection process the Lagrangian cells are considered to be isolated parcels of air. However, in reality the air is mixed with other parcels by diffusion processes characteristic of the size of a parcel. In this model the mixing ratio of a species in a parcel c is brought closer to the average background mixing ratio $\bar{c}$ by adding a term $(\bar{c} - c)d$, where d is a parameter representing the degree of exchange taken to be 10^{-3} in the troposphere and 10^{-6} in the stratosphere (the division is taken arbitrarily to be at $\eta = 0.4$). We estimate $\bar{c}$ to be the average mixing ratio of all the cells within a grid volume, which are chosen to be $5^\circ \times 5^\circ \times \Delta\eta = 0.1$

as this gives an average of about one and a half cells per grid volume (more near the equator, less near the poles). The volumes are fixed to the Eulerian grid. The exchange is treated in a more theoretical manner by Walton *et al.* (1988).

2.2. BOUNDARY-LAYER HEIGHT

The height of the boundary layer in our model is estimated from the archived Unified Model meteorological data in two ways based on a study by Maryon and Best (1992). The first is a dry adiabatic method. This involves following the dry adiabatic lapse rate curve up from the near-surface temperature and determining the height at which it intersects the environmental temperature profile. The second is a Richardson number method where the boundary-layer height is taken to be the first model layer at which the bulk Richardson number exceeds a critical value. The critical value is usually taken as +0.25 but we use +1.3 as chosen by Maryon and Best (1992) which is more appropriate for the Unified Model output. The boundary-layer height used is from the method giving the higher value. In practice the dry adiabatic method tends to be chosen in convective situations and the Richardson number method in stable situations.

2.3. CHEMISTRY

There are 50 species in the model including the main trace gas species which are thought to influence the tropospheric ozone budget: methane, carbon monoxide, hydrogen, ozone, nitric oxide and nitrogen dioxide, and nine nonmethane volatile organic compounds. A wide range of atomic and free radical species have been incorporated in the model, including organic peroxy, alkoxy and carbonyl compounds formed by hydrocarbon oxidation. Obviously with finite resources we had to be discriminating in our choice of model species and neglect those which do not contribute significantly to chemical regimes we wish to model, for instance we have not included either HONO or HNO_4, the former is important in urban-scale smog chemistry which we cannot represent with the spatial resolution of our model, whereas the latter is thermally unstable and only important in the cold upper troposphere away from the region of interest in this study and where the NO_X levels are determined largely by stratospheric input.

The model species are produced and destroyed in reactions and photochemical dissociations, the rate coefficients for which are specified as functions of temperature and incident light, respectively. At present the model includes 90 chemical reactions (see Table III) and 16 photochemical reactions (see Table IV), perfect mixing within a parcel is assumed. The concentration of each chemical species is updated using a backward Euler integration with a chemical timestep, Δt, set at 5 minutes in the present study.

The rate coefficient data for the chemical reactions in Table III were taken from literature data evaluations. The data for the reactions of the atoms, molecules and

Table III. Reactions used in the chemistry model. Rate coefficients are in molecules^{-1} cm^3 s^{-1}, except K_{255} and K_{256} which are in s^{-1}. Rates are listed as complex when there is no simple exponential temperature dependence

$O(^3P) + O_2 + M$	→	$O_3 + M$	$K_1 = 6.0 \times 10^{-34}(T/300)^{-2.3}$
$O(^3P) + NO + M$	→	$NO_2 + M$	K_5 complex
$O(^1D) + N_2$	→	$O(^3P) + N_2$	$K_{7a} = 3.2 \times 10^{-11}$ exp(70/T)
$O(^1D) + O_2$	→	$O(^3P) + O_2$	$K_{7b} = 1.8 \times 10^{-11}$ exp(110/T)
$H_2O + O(^1D)$	→	2OH	$K_8 = 2.2 \times 10^{-10}$
$NO + O_3$	→	$NO_2 + O_2$	$K_{11} = 2.0 \times 10^{-12}$ exp(-1400/T)
$NO_2 + O_3$	→	$NO_3 + O_2$	$K_{12} = 1.2 \times 10^{-13}$ exp(-2450/T)
$OH + O_3$	→	$HO_2 + O_2$	$K_{13} = 1.6 \times 10^{-12}$ exp(-940/T)
$HO_2 + O_3$	→	$OH + 2O_2$	$K_{14} = 1.1 \times 10^{-14}$ exp(-500/T)
$NO + NO_3$	→	$2NO_2$	$K_{15} = 1.1 \times 10^{-11}$ exp(170/T)
$HO_2 + NO$	→	$OH + NO_2$	$K_{17} = 3.7 \times 10^{-12}$ exp(250/T)
$NO_2 + NO_3$	→	$NO + NO_2 + O_2$	$K_{19} = 4.5 \times 10^{-14}$ exp(-1260/T)
$NO_2 + NO_3 + M$	→	$N_2O_5 + M$	K_{20} complex
$NO_2 + OH + M$	→	$HNO_3 + M$	K_{21} complex
$2NO_3$	→	$2NO_2 + O_2$	$K_{27} = 1.0 \times 10^{-12}$ exp(-2450/T)
$N_2O_5 + M$	→	$NO_2 + NO_3 + M$	K_{29} complex
$OH + HO_2$	→	$H_2O + O_2$	$K_{30} = 4.8 \times 10^{-11}$ exp(250/T)
$H_2O_2 + OH$	→	$HO_2 + H_2O$	$K_{31} = 2.9 \times 10^{-12}$ exp(-160/T)
$NO_3 + H_2O_2$	→	$HNO_3 + HO_2$	$K_{32} = 4.1 \times 10^{-16}$
$H_2 + OH$	→	$HO_2 + H_2O$	$K_{33} = 5.5 \times 10^{-12}$ exp(-2000/T)
$HNO_3 + OH$	→	$NO_3 + H_2O$	K_{35} complex
$2HO_2 + M$	→	$H_2O_2 + O_2 + M$	K_{36} complex
$SO_2 + OH + M$	→	$HO_2 + SA + M$	K_{39} complex
$SO_2 + CH_3O_2$	→	$SA + HCHO + HO_2$	$K_{40} = 4.0 \times 10^{-17}$
$H_2O + N_2O_5$	→	$2HNO_3$	$K_{42} = 2.0 \times 10^{-21}$
$OH + CH_4 + O_2$	→	$CH_3O_2 + H_2O$	$K_{59} = 2.9 \times 10^{-12}$ exp(-1820/T)
$CH_3O_2 + NO$	→	$HCHO + HO_2 + NO_2$	$K_{60} = 4.2 \times 10^{-12}$ exp(180/T)
$2CH_3O_2$	→	$2HCHO + 2HO_2$	K_{61} complex
$2CH_3O_2$	→	2HCHO	K_{62} complex
$CH_3O_2 + HO_2$	→	CH_3O_2H	$K_{65} = 4.1 \times 10^{-13}$ exp(790/T)
$HCHO + OH$	→	$HO_2 + CO$	$K_{66} = 1.0 \times 10^{-11}$
$NO_3 + HCHO$	→	$HNO_3 + CO + HO_2$	$K_{67} = 5.8 \times 10^{-16}$
$CO + OH$	→	$HO_2 + CO_2$	K_{70} complex
$C_2H_6 + OH$	→	$C_2H_5O_2$	$K_{71} = 7.8 \times 10^{-12}$ exp(-1020/T)
$NO + C_2H_5O_2$	→	$CH_3CHO + HO_2 + NO_2$	$K_{72} = 4.9 \times 10^{-12}$ exp(180/T)
$CH_3O_2 + C_2H_5O_2$	→	$2HO_2 + HCHO + CH_3CHO$	$K_{73} = 1.0 \times 10^{-13}$
$CH_3CHO + OH$	→	CH_3COO_2	$K_{75} = 5.6 \times 10^{-12}$ exp(310/T)
$CH_3COO_2 + NO_2 + M$	→	PAN + M	K_{77} complex
PAN + M	→	$CH_3COO_2 + NO_2 + M$	K_{78} complex
$NO + CH_3COO_2$	→	$CH_3O_2 + NO_2$	$K_{79} = 2.0 \times 10^{-11}$
$CH_3O_2 + CH_3COO_2$	→	$HO_2 + HCHO + CH_3O_2 + CO_2$	K_{80} complex
$nC_4H_{10} + OH$	→	$secC_4H_9O_2$	$K_{81} = 1.5 \times 10^{-17}T^2$ exp(190/T)
$NO + secC_4H_9O_2$	→	$HO_2 + NO_2 + CH_3COC_2H_5$	K_{83a} complex
	→	$NO_2 + C_2H_5O_2 + CH_3CHO$	K_{83b} complex
$CH_3O_2 + secC_4H_9O_2$	→	$2HO_2 + HCHO + CH_3COC_2H_5$	K_{84a} complex
	→	$HO_2 + CH_3CHO + HCHO + C_2H_5O_2$	K_{84b} complex
$CH_3COC_2H_5 + OH$	→	$CH_3COCHO_2CH_3$	$K_{86} = 3.24 \times 10^{-17}T^2$ exp(414/T)
$2C_2H_5O_2$	→	$2CH_3CHO + 2HO_2$	K_{90} complex
$2CH_3COO_2$	→	$2CH_3O_2 + 2CO_2 + O_2$	$K_{91} = 2.8 \times 10^{-12}$ exp(530/T)
$CH_3COO_2 + CH_3O_2$	→	$2HCHO + O_2$	$K_{92} = 1.0 \times 10^{-13}$
$NO + CH_3COCHO_2CH_3$	→	$HO_2 + CH_3COCOCH_3 + NO_2$	$K_{105} = 5.0 \times 10^{-12}$
$CH_3O_2 + CH_3COCHO_2CH_3$	→	$HCHO + CH_3COCOCH_3 + 2HO_2$	K_{106} complex
$C_2H_4 + OH + M$	→	$CH_2O_2CH_2OH + M$	K_{109} complex
$NO + CH_2O_2CH_2OH$	→	$HO_2 + 2HCHO + NO_2$	$K_{110} = 9.0 \times 10^{-12}$
$CH_3O_2 + CH_2O_2CH_2OH$	→	$3HCHO + 2HO_2$	$K_{111} = 1.0 \times 10^{-13}$
$C_2H_4 + O_3$	→	$CO + 2HO_2 +$ products	$K_{112} = 1.2 \times 10^{-14}$ exp(-2630/T)
$O_3 + C_3H_6$	→	$HCHO + CH_3O_2 + CO + HO_2$	$K_{123} = 4.0 \times 10^{-15}$ exp(-1900/T)
$O_3 + C_3H_6$	→	$CO + CH_3CHO + HO_2$	$K_{124} = 2.6 \times 10^{-15}$ exp(-1900/T)

Table III. *(Continued)*

$OH + C_3H_6 + M$	→	$CH_3CHO_2CH_2OH + M$	K_{125} complex
$NO + CH_3CHO_2CH_2OH$	→	$HCHO + CH_3CHO + HO_2 + NO_2$	$K_{126} = 9.0 \times 10^{-12}$
$CH_3O_2 + CH_3CHO_2CH_2OH$	→	$2HCHO + CH_3CHO + HO_2$	$K_{127} = 1.0 \times 10^{-13}$
$CH_4 + NO_3$	→	$HNO_3 + CH_3O_2$	$K_{200} = 1.0 \times 10^{-18}$
$C_2H_6 + NO_3$	→	$HNO_3 + C_2H_5O_2$	$K_{201} = 1.4 \times 10^{-18}$
$nC_4H_{10} + NO_3$	→	$HNO_3 + secC_4H_9O_2$	$K_{202} = 6.6 \times 10^{-17}$
$C_2H_4 + NO_3$	→	$NO_3C_2H_4O_2$	$K_{203} = 5.43 \times 10^{-12}$ exp(-3401/T)
$NO_3C_2H_4O_2 + NO$	→	nitrate aerosol $+ HO_2 + NO_2$	$K_{204} = 1.4 \times 10^{-11}$ exp(-180/T)
$C_3H_6 + NO_3$	→	$NO_3C_3H_6O_2$	$K_{205} = 9.45 \times 10^{-15}$
$NO_3C_3H_6O_2 + NO$	→	nitrate aerosol $+ HO_2 + NO_2$	$K_{206} = 1.4 \times 10^{-11}$ exp(-180/T)
$CH_3CHO + NO_3$	→	$HNO_3 + CH_3COO_2$	$K_{208} = 1.44 \times 10^{-12}$ exp(-1862/T)
$C_5H_8 + NO_3$	→	$NO_3C_5H_8O_3$	$K_{209} = 3.03 \times 10^{-12}$ exp(-440/T)
$NO_3C_5H_8O_3 + NO$	→	nitrate aerosol $+ HO_2 + NO_2$	$K_{210} = 1.4 \times 10^{-11}$ exp(-180/T)
o-xylene $+ NO_3$	→	$NO_3C_6H_4(CH_3)_2O_2$	$K_{211} = 3.8 \times 10^{-16}$
$NO_3C_6H_4(CH_3)_2O_2 + NO$	→	nitrate aerosol $+ HO_2 + NO_2$	$K_{212} = 1.4 \times 10^{-11}$ exp(-180/T)
$NO + HOC_6H_5CH_3O_2$	→	methyl maleic dialdehyde + glyoxal + $HO_2 + NO_2$	$K_{213} = 4.1 \times 10^{-12}$
o-xylene + OH	→	$HOC_6H_4(CH_3)_2O_2$	$K_{230} = 1.37 \times 10^{-11}$
$NO + HOC_6H_4(CH_3)_2O_2$	→	HO_2 + methyl glyoxal + methyl maleic dialdehyde $+ NO_2$	$K_{231} = 4.0 \times 10^{-12}$
methyl maleic dialdehyde + OH	→	$CHOCH(OH)CO_2CH_3CHO$	$K_{232} = 5.6 \times 10^{-11}$
$CHOCH(OH)CO_2CH_3CHO + NO$	→	HO_2 + methyl glyoxal + glyoxal $+ NO_2$	$K_{233} = 9.0 \times 10^{-12}$
OH + toluene	→	$HOC_6H_5CH_3O_2$	$K_{234} = 5.96 \times 10^{-12}$
$HOC_6H_4(CH_3)_2O_2 + CH_3O_2$	→	$2HO_2 + HCHO$ + methyl glyoxal + methyl maleic dialdehyde	$K_{240} = 1.0 \times 10^{-13}$
$CHOCH(OH)CO_2CH_3CHO + CH_3O_2$	→	$2HO_2 + HCHO$ + methyl glyoxal + glyoxal	$K_{241} = 1.0 \times 10^{-13}$
$HOC_5H_8O_2 + CH_3O_2$	→	$2HO_2 + HCHO$ + methyl vinyl ketone	$K_{242} = 1.0 \times 10^{-13}$
$CH_3COCH(O_2)CH_2OH + CH_3O_2$	→	$2HO_2 + HCHO$ + methyl glyoxal	$K_{243} = 1.0 \times 10^{-13}$
$C_5H_8 + OH$	→	$HOC_5H_8O_2$	$K_{251} = 2.54 \times 10^{-11}$ exp(410/T)
$NO + HOC_5H_8O_2$	→	$HCHO + MVK + HO_2 + NO_2$	$K_{252} = 1.4 \times 10^{-11}$ exp(-180/T)
OH + methyl vinyl ketone	→	$CH_3COCH(O_2)CH_2OH$	$K_{253} = 4.13 \times 10^{-12}$ exp(452/T)
$NO + CH_3COCH(O_2)CH_2OH$	→	$HO_2 + HCHO$ + methyl glyoxal $+ NO_2$	$K_{254} = 1.4 \times 10^{-11}$ exp(-180/T)
SO_2	→	sulphate aerosol	$K_{255} = 2.77 \times 10^{-6}$
sulphate aerosol	→	wet removal	$K_{256} = 1.16 \times 10^{-6}$

free radicals derived from O, H, N, CO and SO_2 were taken from Atkinson *et al.* (1992) and for the hydrocarbon degradation reactions from Atkinson (1994). The reaction $SO_2 \xrightarrow{H_2O(\ell)}$ Sulphate Aerosol is given a constant reaction rate of $0.01 hr^{-1}$ (Eliassen *et al.*, 1982).

We have not yet included the heterogeneous reaction of $N_2O_5 + H_2O$ on aerosol, but we do instead include a reaction of N_2O_5 with gaseous water. This reaction gives a removal rate for N_2O_5 of around $2–6 \times 10^{-4}$ s^{-1} in midlatitudes, increasing to over 1×10^{-3} s^{-1} at the equator. The mid-latitude rates are comparable to those of Dentener and Crutzen (1993) calculated for their aerosol reaction given the uncertainties in aerosol distributions. Near the equator our high rate of N_2O_5 removal should account for any wet deposition, however this effect is unimportant as there is very little N_2O_5 present here due to the distance from sources and the high temperatures.

Table IV. Photochemical reactions, and their photolysis rate coefficients, that are implemented in the 3D chemistry model, with sample values in s^{-1} for a solar zenith angle of 15°, with a cloudless sky, over land, 350 Dobson Units of ozone, at an altitude of 0.5 km

$O_3 + h\nu$	$\rightarrow$	$O(^3P) + O_2$	($\lambda > 300$ nm)	$J_1 = 4.76 \times 10^{-4}$
$O_3 + h\nu$	$\rightarrow$	$O(^1D) + O_2$	($\lambda < 317$ nm)	$J_2 = 3.24 \times 10^{-5}$
$NO_2 + h\nu$	$\rightarrow$	$O(^3P) + NO$		$J_3 = 9.00 \times 10^{-3}$
$H_2O_2 + h\nu$	$\rightarrow$	$2OH$		$J_4 = 7.98 \times 10^{-6}$
$HNO_3 + h\nu$	$\rightarrow$	$OH + NO_2$		$J_5 = 7.12 \times 10^{-7}$
$HCHO + h\nu$	$\rightarrow$	$CO + 2HO_2$		$J_6 = 3.30 \times 10^{-5}$
$HCHO + h\nu$	$\rightarrow$	$CO + H_2$		$J_7 = 4.99 \times 10^{-5}$
$CH_3CHO + h\nu$	$\rightarrow$	$CO + CH_3O_2 + HO_2$		$J_8 = 5.16 \times 10^{-6}$
$CH_3COC_2H_5 + h\nu$	$\rightarrow$	$CH_3COO_2 + C_2H_5O_2$		$J_9 = 4.20 \times 10^{-6}$
$CH_3COCOCH_3 + h\nu$	$\rightarrow$	$2CH_3COO_2$		$J_{10} = 2.75 \times 10^{-4}$
methyl glyoxal + $h\nu$	$\rightarrow$	$CO + CH_3COO_2 + HO_2$		$J_{11} = 1.28 \times 10^{-4}$
glyoxal + $h\nu$	$\rightarrow$	$HCHO + CO$		$J_{12} = 5.76 \times 10^{-5}$
$NO_3 + h\nu$	$\rightarrow$	$O_2 + NO$		$J_{13} = 2.39 \times 10^{-2}$
$NO_3 + h\nu$	$\rightarrow$	$O(^3P) + NO_2$		$J_{14} = 1.64 \times 10^{-1}$
$N_2O_5 + h\nu$	$\rightarrow$	$NO_2 + NO_3$		$J_{15} = 4.61 \times 10^{-5}$
$CH_3O_2H + h\nu$	$\rightarrow$	$HCHO + OH + HO_2$		$J_{16} = 4.36 \times 10^{-6}$

2.4. PHOTOLYSIS

The photochemical reactions that we have included in our 3D Lagrangian tropospheric chemistry model are listed in Table IV. The photolysis rate (J_X) for a species (X) is the product of the spherically integrated (actinic) flux (F) with the absorption cross-section (σ) and the quantum yield (ϕ), integrated over all wavelengths (λ).

$$J_X = \int_0^\infty F(\lambda)\sigma_X(\lambda)\phi_X(\lambda)\mathrm{d}\lambda. \tag{3}$$

The quantum yield is the probability of the species dissociating after absorbing a photon. In practice, the integral is restricted to the range in which the integrand is significant and the integral itself is replaced by a sum over wavelength intervals.

The cross-sections and quantum yields for the reactions have been obtained from a variety of sources (Burkholder *et al.*, 1993; Atkinson *et al.*, 1992; NASA, 1992; Martinez *et al.*, 1992; Nicovitch and Wine, 1988; Rattigan *et al.*, 1992; WMO, 1986). The actinic flux is affected by a large number of factors. The solar flux incident on the atmosphere is attenuated by ozone and molecular oxygen absorption. The remaining flux reaching the troposphere is scattered by aerosols, clouds and atmospheric molecules and is reflected by the Earth's surface. Thus the light incident on any air parcel has arrived by many different and tortuous paths. The algorithm used to calculate the spherically integrated solar flux is an adaptation of the one-dimensional two stream model (upward and downward fluxes) developed by Hough (1988).

2.4.1. *Parameterising the Photolysis Results for Incorporation into the 3-D Chemistry Model*

Ideally we would like to be able to calculate the flux exactly and integrate according to Equation (3), but to do this for the 50 000 air parcels for every 5 minute timestep would be prohibitive in terms of computing time. We are fortunate that most of the variables on which the photolysis rates depend only vary slowly with time. The factors that affect the photolysis rates are; solar flux, aerosol content, stratospheric oxygen and ozone columns, tropospheric oxygen and ozone profiles, surface albedo, cloud cover, height above surface, and solar zenith angle. Of these, only the solar zenith angle and the cloud cover vary on a diurnal basis; the rest have a characteristic timescale of a year. Values of $\sec\theta$ are calculated for each air parcel at every chemical time step from its latitude, longitude and time of day.

2.4.2. *Parameterisation as a Function of Zenith Angle*

The photolysis rates have a very strong dependence on solar zenith angle. The effect of attenuating molecules and aerosols is to reduce the direct flux by a factor $\exp(\text{constant} \times \sec\theta)$. So a reasonable guess at a parameterisation is:

$$J = \mathcal{A} \times \exp(-\mathcal{B} \times \sec\theta), \tag{4}$$

where θ is the zenith angle and $\mathcal{A}$ and $\mathcal{B}$ are chosen to get the best approximation to the explicitly calculated photolysis rates. The values for $\mathcal{A}$ and $\mathcal{B}$ will be different for different photolysis reactions. This is obvious for the scale factor $\mathcal{A}$. The θ-dependence, given by $\mathcal{B}$, will be determined by the variations of cross-sections and quantum yields with wavelength, as the different scattering and absorption processes affect the different wavelengths to a greater or lesser extent. For each reaction, $\mathcal{A}$ and $\mathcal{B}$ are calculated by constraining the parameterised J value at midday local time to be equal to the explicitly calculated one, and constraining the integrals under the parameterised and explicit curves over the entire 24 hour interval to be equal. The first condition guarantees that for overhead sun, when photolysis reactions are at their fastest, the parameterisation is exact. The second condition ensures that when the sun travels over the range of zenith angles in a day the flux of molecules through the reaction in that day is also exact.

2.4.3. *Implementation in the Model*

A 72×36 grid (5° square) on nine levels spaced by $\Delta\eta = 0.1$ is used when calculating the parameters $\mathcal{A}$ and $\mathcal{B}$ for equation 4 as described in Section 2.4.2. For each grid square the $\mathcal{A}$s and $\mathcal{B}$s for each reaction and for each level are calculated, taking into account the stratospheric ozone column, the surface albedo, the cloud cover and the variation of solar zenith angle with time of day. The aerosol and oxygen profiles are global averages fixed for all grid squares and are taken from Hough (1988). The stratospheric ozone is taken from a monthly 2-D climatology.

The tropospheric ozone profile is calculated within the model. We have used the parameterisation from Hough (1988) to calculate the surface albedo.

The cloud data are taken from the Meteorological Office global rolling archive as an 18-day average of high, medium, low and convective cloud. These are converted to physically thin (but may be optically thick) partially scattering layers in a $5^\circ \times 5^\circ \times 9$ level array.

The range of zenith angles is calculated for the latitude of the centre of the grid square and the fitting procedure is used as described in Section 2.4.2.

2.5. EMISSIONS

Emissions into the model are implemented as an additional term in the production flux for the species rather than as a step change in species concentration after a chosen timestep. The emissions used are listed in Table V. The anthropogenic, biomass burning, vegetation, soil, oceans and 'other' are all surface sources based on two-dimensional (latitude, longitude) source maps. Stratospheric sources of ozone and nitric acid are calculated as two-dimensional inputs into the top model layer. The aircraft and lightning NO_X sources are three-dimensional. We use the term 'anthropogenic' in this paper to describe direct emissions from fossil fuel combustion, although man will also have a large influence on biomass burning and (through farming) on vegetation, paddies and animal sources. Aircraft are not included in the 'anthropogenic' emissions but are treated separately. The anthropogenic, paddy, tundra, wetland and 'other animal' sources (see Table V) are based on a yearly average and are constant throughout the year. The other sources vary by calendar month.

The methane emissions in Table V were based on the IPCC (1995) assessment and a total source strength of 485 Tg yr^{-1}. The spatial distributions of the oceans, tundra and wetland sources were estimated from the corresponding distributions of biospheric zones (Olson and Watts, 1982); anthropogenic sources were given the same distribution as NO_X emissions (Benkovitz *et al.*, 1996, in preparation) and biomass burning as that of SO_2 from the same source (Spiro *et al.*, 1992).

Global hydrocarbon emissions from vegetation sources were taken from Hough (1991) and were distributed in space and time as for dimethyl sulphide from the corresponding soil and vegetation sources (Spiro *et al.*, 1992). Soil NO_X emissions were taken from Yienger and Levy (1995)

The entries in Table V for carbon monoxide are based on the literature review by Warneck (1988). Biomass burning and human activities, mainly the exhausts of petrol-engined vehicles, are the largest contributors. This table does not account for the carbon monoxide produced by hydrocarbon oxidation which our study shows to be a somewhat larger secondary source than any of the direct primary emissions. The spatial distribution of the anthropogenic sources was taken to be the same as that for NO_X (Benkovitz *et al.*, in preparation) and biomass burning from Spiro *et al.* (1992).

Table V. Emissions in Tg yr^{-1}, except NO_x and HNO_3, which are in Tg (N) yr^{-1}, and SO_2, which are in Tg (S) yr^{-1}. The 'Other' for methane includes paddys (60 Tg yr^{-1}), tundra (50 Tg yr^{-1}), wetlands (65 Tg yr^{-1}), termites (20 Tg yr^{-1}) and other animals (85 Tg yr^{-1}). The emissions for n-C_4H_{10} are increased to compensate for the emissions of longer chain alkanes, no adjustment for their different molecular masses is made and the emission rates in this table are assumed by our model to be in Tg of n-C_4H_{10} yr^{-1}

Species	Source								
	Anthro-pogenic	Biomass burning	Vege-tation	Soil	Oceans	Air-craft	Light-ning	Strato-sphere	Other
NO_x	21.0	8.0	–	5.0	–	0.85	5.0	–	–
SO_2	65.1	2.2	–	–	15.0	–	–	–	–
HCHO	1.0	–	–	–	–	–	–	–	–
H_2	20.0	20.0	–	5.0	5.0	–	–	–	–
CH_3CHO	0.3	–	–	–	–	–	–	–	–
CO	650.0	800.0	75.0	–	50.0	–	–	–	–
CH_4	155.0	40.0	–	–	10.0	–	–	–	280.0
C_2H_6	6.0	6.5	3.5	–	–	–	–	–	–
n-C_4H_{10}	47.0	2.0	8.0	–	–	–	–	–	–
C_2H_4	17.0	10.0	20.0	–	–	–	–	–	–
C_3H_6	21.0	5.0	20.0	–	–	–	–	–	–
C_5H_8	–	–	506.0	–	–	–	–	–	–
o-xylene	4.7	–	–	–	–	–	–	–	–
toluene	14.0	–	–	–	–	–	–	–	–
HNO_3	–	–	–	–	–	–	–	0.45	–
O_3	–	–	–	–	–	–	–	450.0	–

The principle source of the oxides of nitrogen is fossil fuel combustion and Table V reflects this situation (Logan, 1983; Dignon and Hameed, 1989). The spatial distribution was taken directly from Benkovitz *et al.* (in preparation).

Although SO_2 gas-phase chemistry has little or no effect on ozone production we have included SO_2 as a species in our model to allow future study. We do not have a DMS oxidation scheme so all DMS emissions are emitted into our model as SO_2. This has no effect on the present work.

2.5.1. *Model Treatment of Surface Emissions*

In our model, surface emissions are added on a $5^\circ \times 5^\circ$ grid square basis. This is too coarse ($\sim$600$\times$400 km at mid-latitudes) to resolve individual centres of pollution but is large enough to give an average cell occupancy of approximately two Lagrangian cells within the boundary layer per grid square in the mid-latitudes. After each advection timestep the surface emissions for a grid square are distributed equally over all the Lagrangian cells that are within the boundary layer in that grid square. If there are no cells within the boundary layer for a particular grid square then the emissions are stored until a cell does pass through.

2.5.2. *Isoprene*

Isoprene is emitted by vegetation during the day, with the emission rate being positively correlated with temperature (Jacob and Wofsy, 1988). In our model we use the simple approach of emitting isoprene at a rate proportional to the cosine of the solar zenith angle during the day, with no emission at night. The rate is adjusted to give the appropriate total emission over a month for each grid square. These monthly emissions were taken from Guenter *et al.* (1995).

2.5.3. *Lightning and Aircraft*

Lightning is an important NO_X source in the free troposphere (Turman and Edgar, 1982; Franzblau and Popp, 1989). We used a parameterisation from Price and Rind (1992) based on model-simulated monthly two-dimensional fields of convective cloud top heights. The emissions were distributed evenly by mass in the vertical between the ground and the convective cloud tops. The total was normalised to give a yearly emission of 5 Tg of N, emitted as NO. In comparison, Strand and Hov (1994) suggest a total of 8 Tg yr^{-1} of N emitted in the regions of outflow from thunderclouds rather than distributed evenly in the vertical. The lightning emissions are calculated on a $5^\circ \times 5^\circ \times \Delta\eta = 0.1$ grid. If there are no Lagrangian cells within a grid volume then the emissions in the other volumes are increased to give the correct global emission every timestep.

For the NO_X emissions from civil and military aircraft three-dimensional emissions fields were used (Schumann, 1995) which amounted to 0.85 Tg yr^{-1} of N globally. These are put into the model using the same procedure as for lightning.

2.5.4. *Stratospheric Sources*

The cells in our model are constrained to remain below $\sim$100hPa by imposing a fixed lid to the model, in reality they would travel to and from the stratosphere bringing high ozone and NO_Y concentrations down to the troposphere and losing species into the stratosphere. Murphy and Fahey (1994) estimate an ozone flux of 450 Tg yr^{-1} from the stratosphere and an NO_Y (NO_Y = NO + NO_2 + HNO_3 + PAN + $2N_2O_5$) flux of 0.45 Tg (N) yr^{-1}. The upper boundary of our model is set at $\eta = 0.1$ ($\sim$100 hPa) and so the vertical windfields are used to calculate an ozone flux across the $\eta = 0.1$ surface on a $5^\circ \times 5^\circ$ grid. We neglect any loss in species due to upwards transport into the stratosphere. Monthly zonal mean ozone fields are taken from Hough and Woods (1988) and interpolated to give the ozone mass mixing ratio at 98.5 hPa, which is used to calculate the stratospheric flux. This pressure level was chosen as it gives a total ozone flux of 450 Tg over one year. The NO_Y flux is taken to be one thousandth of the ozone flux by mass (as N) and is emitted into the model as HNO_3.

The emissions are calculated on a $5^\circ \times 5^\circ$ grid and distributed equally between all Lagrangian cells that are within a grid square and have η values between 0.2

and 0.1. As with the surface emissions if there are no Lagrangian cells in which to distribute the emissions then the emissions are stored.

2.6. DEPOSITION

For all cells within the boundary layer the species loss flux due to dry deposition is calculated to be $c \times v_d/H$ where c is the species concentration, v_d is the species deposition velocity and H is the height of the boundary layer. The deposition velocities depend on the location of the cell according to whether the cell is over land or ocean and are the values given in Hough (1991) (see Table VI). This simple classification could be extended to include differences between tundra, forest, desert etc. At present there is no parameterisation of ice cover. The sea ice and Antarctica are classified as 'ocean', and all other land ice is classified as 'land'. These velocities are 1 m values chosen specifically for the purposes of global-scale modelling. If we assume that species concentrations at 50 m are representative of those throughout the mixed boundary layer then we can convert the deposition velocities at 1 m to give values at 50 m allowing for aerodynamic resistance.

$$\frac{1}{V_{50}} = \frac{1}{V_1} + \frac{50}{K_z}\,, \tag{5}$$

where V_{50} is the deposition velocity at 50 m, V_1 is the deposition velocity at 1 m and K_z is the effective vertical eddy diffusion coefficient in $\mathrm{m^2 s^{-1}}$ between 1 m and 50 m. K_z is approximated by:

$$K_z = 50 \times \frac{k^2 \overline{U}_{30}}{\log \frac{30}{z_0} \log \frac{50}{1}}\,, \tag{6}$$

where $\overline{U}_{30}$ is the average 30 m wind (the lowest Unified Model layer), k is the Von Kármán constant (0.4) and z_0 is the surface roughness length in m. The roughness lengths are taken to be 2×10^{-4} m over sea and 0.2 m over land. Because the winds are 18-day averages and not diurnally varying, the value for K_z is halved over land during the night to take some account of the increase in the stability of the nocturnal boundary layer.

A more detailed calculation is being developed for the aerodynamic resistance using diurnally varying Monin–Obukhov lengths and surface wind stresses.

The only model species that are removed by wet scavenging are HNO_3, H_2O_2 and sulphate aerosol, and these have a global removal rate below $\eta = 0.7$ of 0.1 $\mathrm{day^{-1}}$.

2.7. MODEL OUTPUT

Although the model itself is Lagrangian, the most useful way to visualise the output is as concentrations on a regular grid. The chosen output grid was $5^\circ \times 5^\circ \times \Delta\eta = 0.1$, as used in the emissions and inter-parcel exchange. The species concentration

Table VI. Deposition velocities (in mm s^{-1}) for all the dry deposited species in the model. Values are effective velocities for 1 m above the surface

Species	Land	Ocean
NO_2	1.0	0.5
SO_2	5.0	1.0
CO	0.3	0
O_3	6.0	1.0
HNO_3	40	10
H_2O_2	10	10
H_2	0.45	0
CH_3O_2H	5.0	5.0
PAN	2.0	0

in each 3-D grid box is taken to be the average of all the cells in that box. To smooth out the distributions near the poles and to fill in holes where there are no cells in a grid box, the grid is convolved with a two-dimensional (longitude-latitude) Gaussian filter with a constant width of 200 km.

As well as the species concentrations it is often useful to see the fluxes through particular reactions. The average flux per cell within each grid box divided by the volume of a cell at a height corresponding to the middle of the box gives the volume-averaged reaction flux in molecules cm^{-3} s^{-1}.

3. Some Model Results

The aim of this model is to simulate global ozone production, the main path for which is the oxidation of hydrocarbon and CO to peroxy radicals. These react with NO to give NO_2 which are subsequently photolysed to give odd oxygen atoms (O^3P). The oxygen atoms then combine with molecular oxygen to give ozone (Leighton, 1961 and Levy, 1971). An example of the series of reactions starting with methane is given below.

$$OH + CH_4 \rightarrow H_2O + CH_3 \quad (7)$$

$$CH_3 + O_2 + M \rightarrow CH_3O_2 + M \quad (8)$$

$$CH_3O_2 + NO \rightarrow NO_2 + CH_3O \quad (9)$$

$$CH_3O + O_2 \rightarrow HCHO + HO_2 \quad (10)$$

$$HO_2 + NO \rightarrow OH + NO_2 \quad (11)$$

$$NO_2 + h\nu \rightarrow NO + O^3P \quad (12)$$

$$O^3P + O_2 + M \rightarrow O_3 + M \quad (13)$$

$$\text{net: } CH_4 + 4O_2 \rightarrow 2O_3 + H_2O + HCHO$$

The nitrogen oxides and odd hydrogen radicals are conserved in this mechanism, so the series of reactions will continue to cycle until they are removed by other means. The most important of these are:

$$NO_2 + OH + M \rightarrow HNO_3 + M \quad (14)$$
$$HO_2 + HO_2 + M \rightarrow H_2O_2 + O_2 + M \quad (15)$$
$$OH + HO_2 \rightarrow H_2O + O_2. \quad (16)$$

The important ozone destroying reactions are:

$$O_3 + h\nu \rightarrow O_2 + O^1D \text{ followed by } O^1D + H_2O \rightarrow 2OH \quad (17)$$
$$O_3 + HO_2 \rightarrow OH + 2O_2 \quad (18)$$
$$O_3 + OH \rightarrow HO_2 + O_2 \quad (19)$$
$$O_3 + NO_2 \rightarrow NO_3 + O_2. \quad (20)$$

Here we have included NO_2 loss as an ozone loss as there is a fast cycling between the two. Similarly we have not considered the conversion of NO to NO_2 through reaction with ozone to be an ozone loss as it is part of the O_3–NO_2 cycle. Reaction (20) will only be an ozone loss if the NO_3 is removed before it can be photolysed.

To understand the production of ozone therefore we must understand the distribution of the precursors; OH radicals, peroxy radicals and oxides of nitrogen. To achieve this the model simulation was run for 16 months May 1994 – August 1995. We will look in detail at the results for two months, February 1995 and August 1995.

3.1. AUGUST

Surface and zonal average species mixing ratios of ozone, NO_X, OH and HO_2 for August are shown in Figures 1a–h. These mixing ratios are the average values over the 5 days 12th–17th August.

The OH surface distribution is mostly zonal, being in a broad band centred about 20° North near where the solar actinic fluxes are highest. The distribution is not significantly affected by the continents except over equatorial Africa and South America where even though the total free radical mixing ratio is increased here (as can be seen in the HO_2 mixing ratio), the isoprene emissions from the forests convert the OH to HO_2 causing minima in the OH mixing ratio.

In the zonal average profile, the increased mixing ratio around $\sim$20° north is the most obvious feature. The mixing ratio (molecular density of OH/molecular density of air) increases monotonically with altitude due mainly to the decrease in the density of air with height. In general terms, the molecular density of OH (molecules per unit volume) shows little variation with height throughout most of the troposphere although there is a broad maximum in the midtroposphere, and a tailing off above 200 hPa where there is less radical production.

The distribution of NO_X near the surface follows the land masses as all the surface sources are land-based (anthropogenic, biomass burning and soils). Above the surface, the sources are from lightning and aircraft. The highest concentrations are found in the industrialised regions in the Northern Hemisphere (East Coast of the United States, Central Europe and South East Asia), and above areas of biomass burning and lightning activity in Brazil, Southern Africa and Australia. The zonal average profile of NO_X shows the vertical extent of the anthropogenic emissions (30°N–60°N) and the natural emissions (30°S–0°S). The major oceans are relatively free of NO_X at the surface as there is no production here but the oxidation to NO_Y and deposition of HNO_3 are still efficient. Higher up in the troposphere the production of NO_X from the photolysis of the stratospheric input of HNO_3 is the most important source, particularly in the northern hemisphere where the photolysis in August is strongest.

The HO_2 radical shows a pattern halfway between the zonal OH and the continental NO_X. This is to be expected since, as we saw with OH, the radical-producing photolysis reactions depend on the solar radiation. However the formation of HO_2 radicals also depends on the presence of hydrocarbon pollutants, in particular through the photolysis of HCHO and methyl glyoxal, therefore the distribution follows the continents much more strongly than OH does. In the tropics there are no peaks corresponding to the biomass burning as there were for NO_X. The zonal average profile of HO_2 shows a maximum at the surface centred about 20° north, as for the OH profile. The mixing ratio decreases with height following the water vapour concentration which controls the concentrations of HO_X = (OH + HO_2 + 2 × H_2O_2).

At the surface in the northern mid-latitudes, the ozone distribution follows that of NO_X and HO_2. There are strong maxima over the eastern United States and Europe and other maxima over South East Asia with small ozone maxima in the regions of biomass burning in the southern sub-tropics. The lifetime of ozone at the surface (a few days) is longer than that of NO_X so the ozone spreads outside the continents more. The major loss for ozone near the surface is dry deposition which is a factor of six less effective over the oceans. The zonal average profile shows a maximum at the surface at the latitude of industrial production and a minimum over the Southern Ocean. The maximum at the top of the troposphere in the Northern Hemisphere is due to stratospheric influx.

Over the tropical continents isoprene emissions are very strong and although there are NO_X source in these regions from soils and biomass burning, the conversion from HO_2 to OH by NO and ozone is not enough to compensate for the rapid conversion of OH to HO_2 by the isoprene oxidation. Hence, minima in OH mixing ratios appear even where there are maxima in HO_2. Over industrial regions NO_X and hydrocarbon emissions are co-located leading to maxima in both OH and HO_2 mixing ratios.

3.2. FEBRUARY

The main differences between the summer and winter time conditions are the distribution of sunlight, and the amount and distribution of emitted species. The sunlight, apart from the effects of clouds, is zonally symmetric, the maximum moving from around 20° north in August to around 20° south in February. The biomass burning contribution moves from south of the equator (central South America and Southern Africa) to just north of the equator (central Africa) but the total remains the same. The Northern Hemisphere mid-latitude emissions from vegetation (the most important of these being isoprene) disappear in February, the African and South American sources move further south, and the Australian vegetation emissions reappear. The stratospheric inputs of ozone and HNO_3 are three times higher in February than in August.

In Central Europe, the boundary layer OH mixing ratios are about a factor of five less in February than in August (compare Figures 1e and f with 2e and f). On a global scale, the higher OH concentrations have shifted to the Southern Hemisphere and there are minima in the distribution over Brazil and Zaire caused by isoprene emissions converting OH to HO_2. There is less OH in the high southern latitudes in February compared to the high northern latitudes in the August because there are few NO_X or hydrocarbon emissions from the Southern Ocean and Antarctica and so ozone or formaldehyde production (ozone and formaldehyde photolysis are the most important sources of OH). The February zonal average profile is almost a mirror image of the August one although there are some differences near the equator as the differences in the land distribution north and south of the equator will affect the convective cloud cover and the convective transport of emissions.

The surface distribution of NO_X (Figure 2c) is largely determined by the emissions where the largest seasonal effect is due to the biomass burning. The large areas of high NO_X concentration over South America, Southern Africa and Australia in Figure 1c have reduced to be replaced by high concentrations in Central Africa and China. The increase in NO_X over the industrial areas of Europe and Russia in February is because the removal processes (involving OH and HO_2) are less efficient, rather than any increase in emission. The zonal average profile (Figure 2d) shows a broad band of high NO_X concentrations in the Northern Hemisphere at lower altitudes rather than the separate maxima for industrial and biomass burning latitudes seen in Figure 1d.

The maxima in the HO_2 distribution (Figure 2g) have shifted into Southern Hemisphere in February. However, unlike the August case, the HO_2 distribution over the continents does not follow the NO_X distribution. It is the volatile organic compounds (VOCs) which convert OH to HO_2. In the Northern Hemisphere the sources of NO_X and VOCs are largely anthropogenic and hence coincident. In the Southern Hemisphere the primary route for OH to HO_2 conversion is through isoprene (reaction 251 in Table III followed by reactions 242, 243, 252 or 253). Isoprene is emitted from vegetation, in February this comes from the forests of

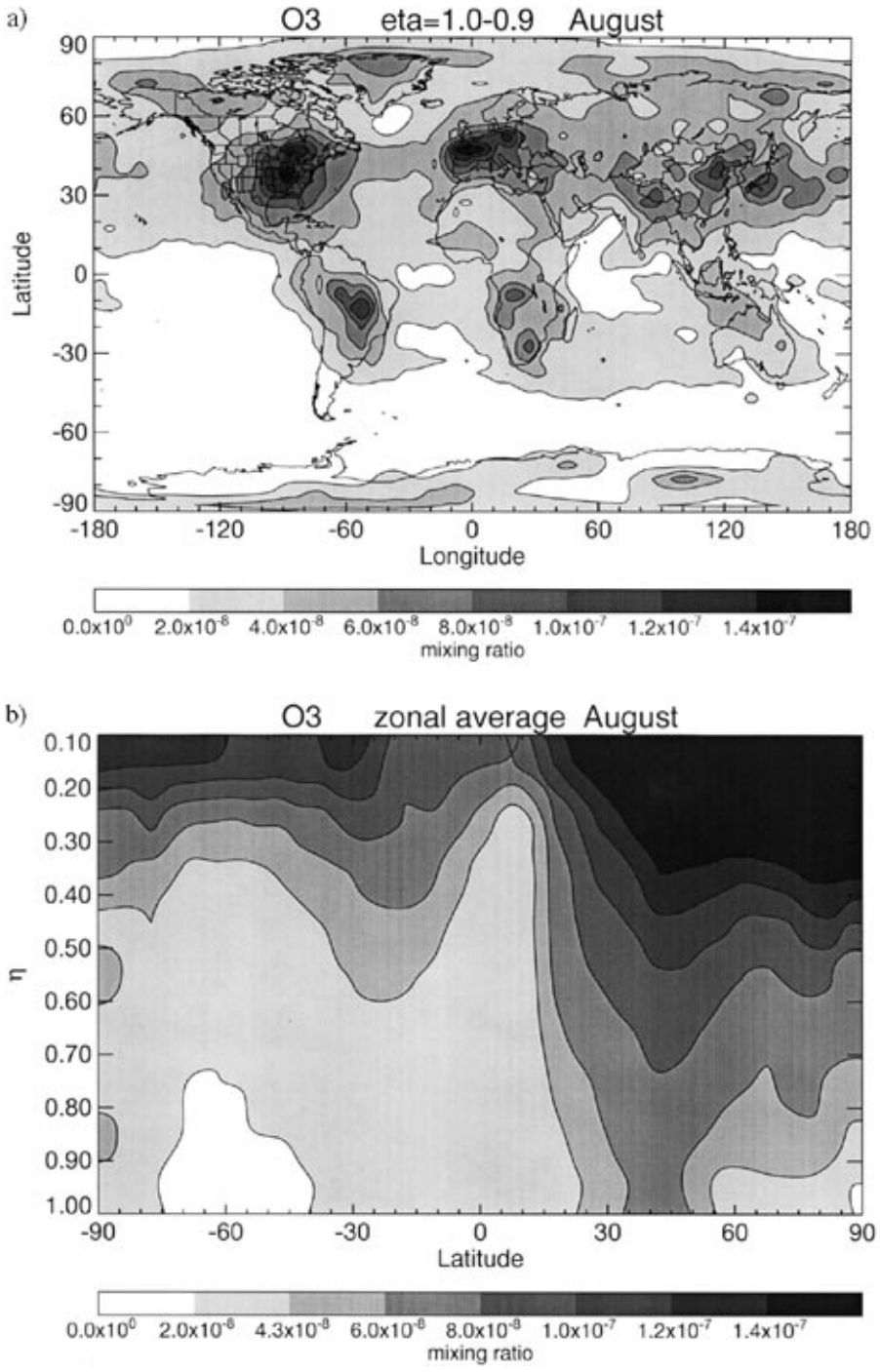
a)
O3 eta=1.0-0.9 August
90
60
30
0
-30
-60
-90
Latitude
-180
-120
-60
0
60
120
180
Longitude
0.0x10^0 2.0x10^-8 4.0x10^-8 6.0x10^-8 8.0x10^-8 1.0x10^-7 1.2x10^-7 1.4x10^-7
mixing ratio
b)
O3 zonal average August
0.10
0.20
0.30
0.40
0.50
0.60
0.70
0.80
0.90
1.00
η
-90
-60
-30
0
30
60
90
Latitude
0.0x10^0 2.0x10^-8 4.3x10^-8 6.0x10^-8 8.0x10^-8 1.0x10^-7 1.2x10^-7 1.4x10^-7
mixing ratio

Figure 1a–1b.

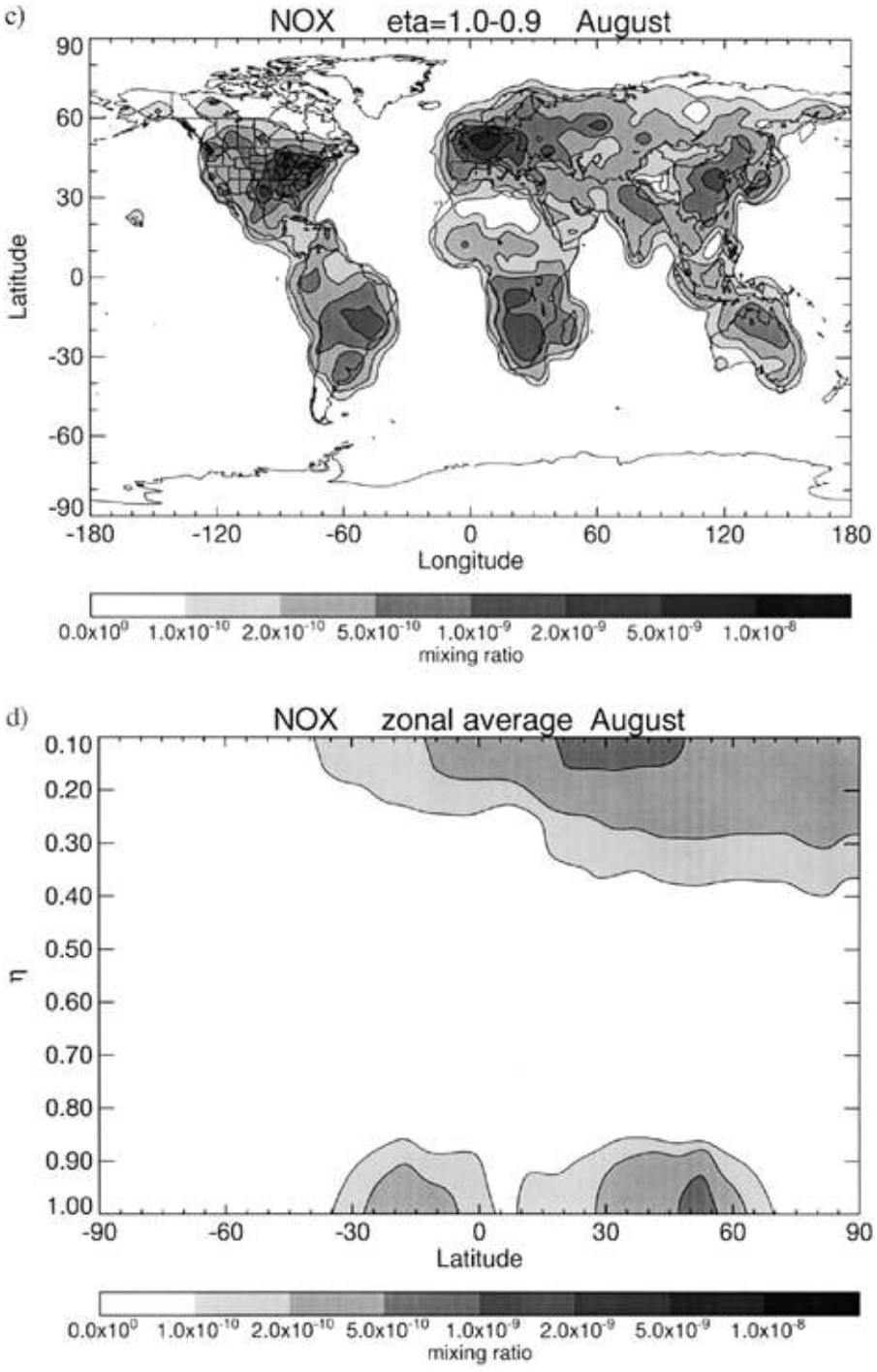
c)
NOX eta=1.0-0.9 August
Latitude
90
60
30
0
-30
-60
-90
-180 -120 -60 0 60 120 180
Longitude
0.0x10^0 1.0x10^-10 2.0x10^-10 5.0x10^-10 1.0x10^-9 2.0x10^-9 5.0x10^-9 1.0x10^-8
mixing ratio
d)
NOX zonal average August
η
0.10
0.20
0.30
0.40
0.50
0.60
0.70
0.80
0.90
1.00
-90 -60 -30 0 30 60 90
Latitude
0.0x10^0 1.0x10^-10 2.0x10^-10 5.0x10^-10 1.0x10^-9 2.0x10^-9 5.0x10^-9 1.0x10^-8
mixing ratio

Figure 1c–1d.

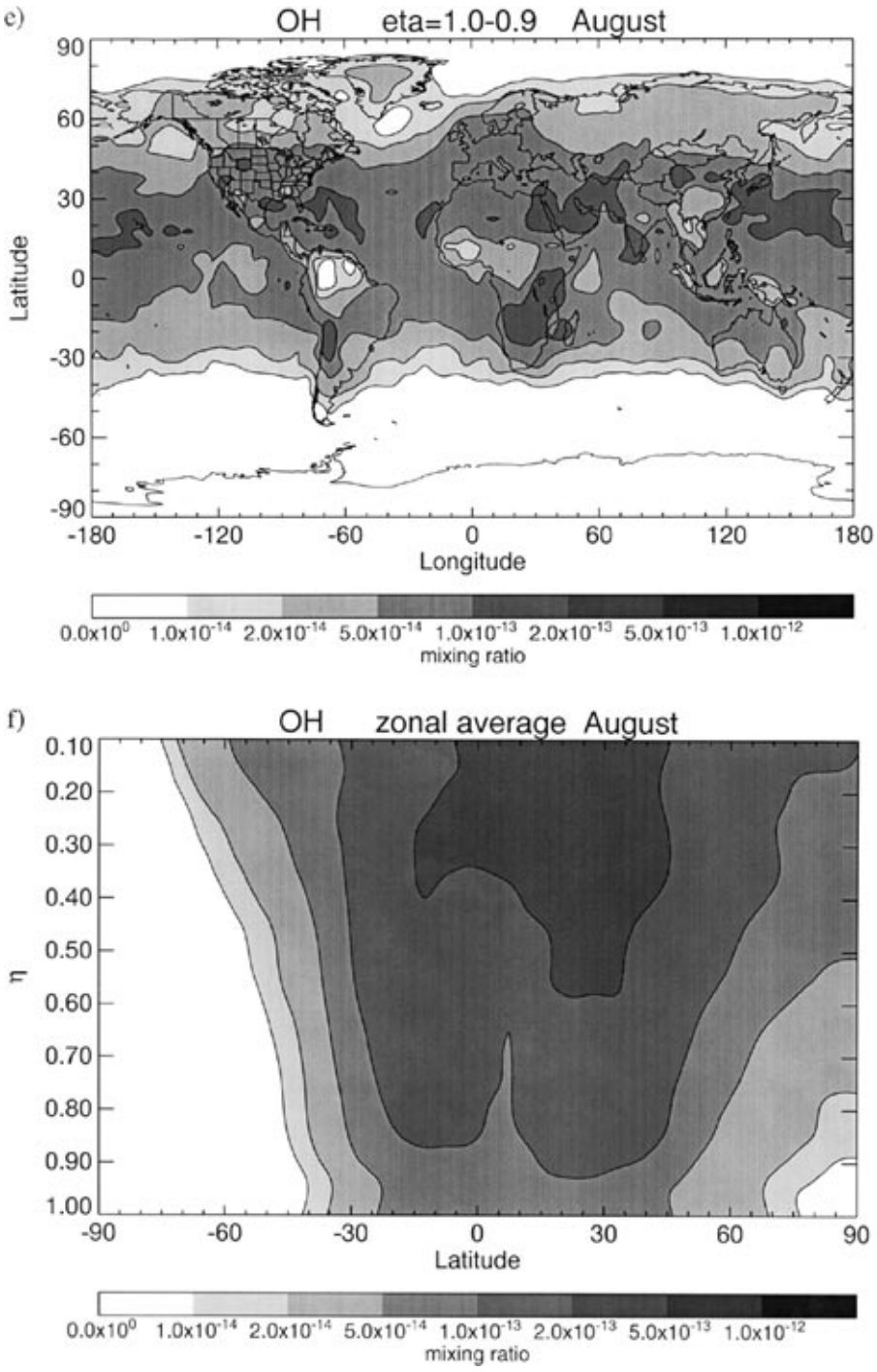
e)
OH eta=1.0-0.9 August
90
60
30
0
-30
-60
-90
Latitude
-180 -120 -60 0 60 120 180
Longitude
0.0x10^0 1.0x10^-14 2.0x10^-14 5.0x10^-14 1.0x10^-13 2.0x10^-13 5.0x10^-13 1.0x10^-12
mixing ratio
f)
OH zonal average August
0.10
0.20
0.30
0.40
0.50
0.60
0.70
0.80
0.90
1.00
η
-90 -60 -30 0 30 60 90
Latitude
0.0x10^0 1.0x10^-14 2.0x10^-14 5.0x10^-14 1.0x10^-13 2.0x10^-13 5.0x10^-13 1.0x10^-12
mixing ratio

Figure 1e–1f.

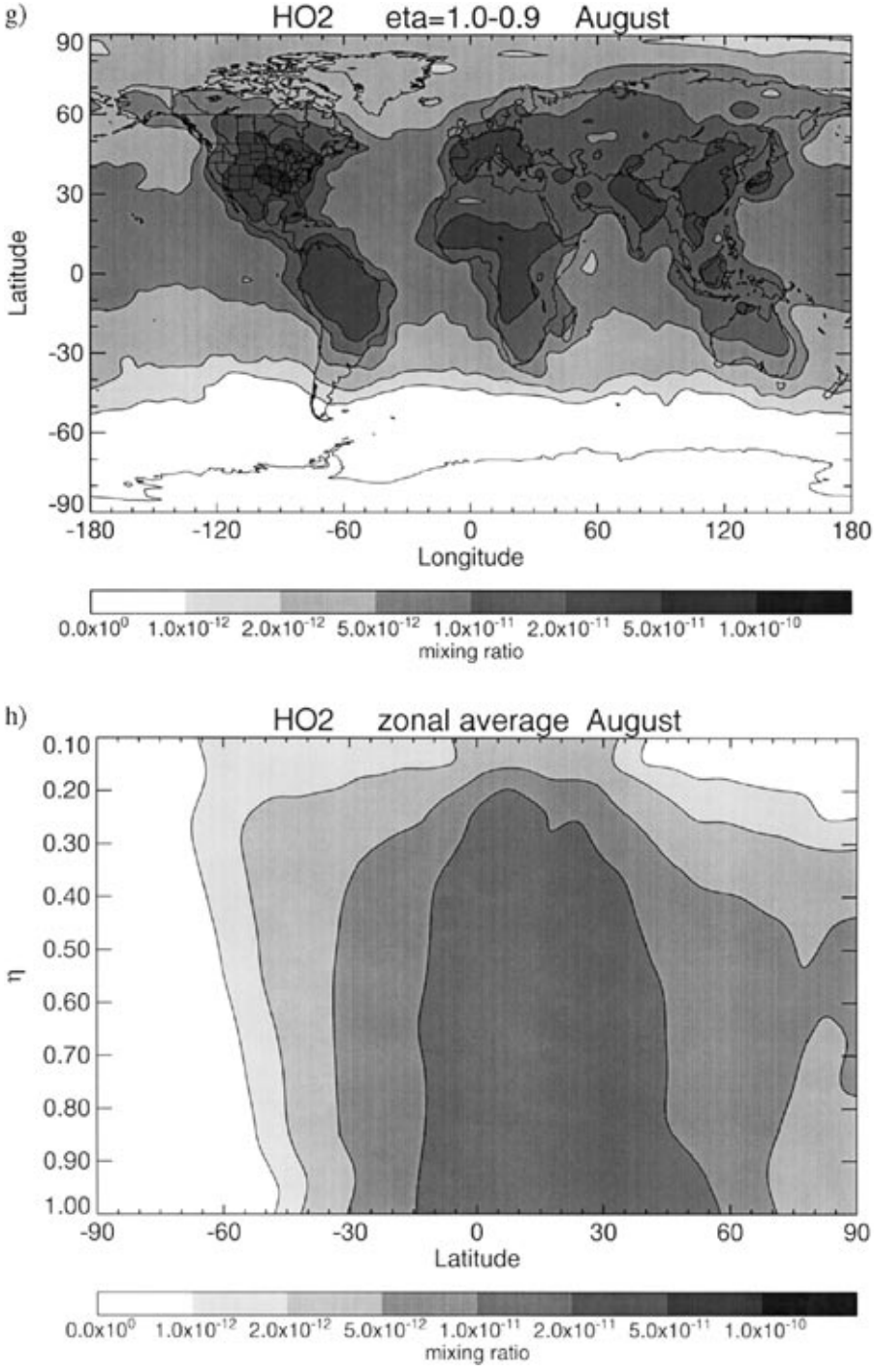

Figure 1g–1h.

Figure 1. Near surface and zonal average profiles of mixing ratios of OH, NO_X, HO_2 and O_3 over the 5 days ending on 17th August.

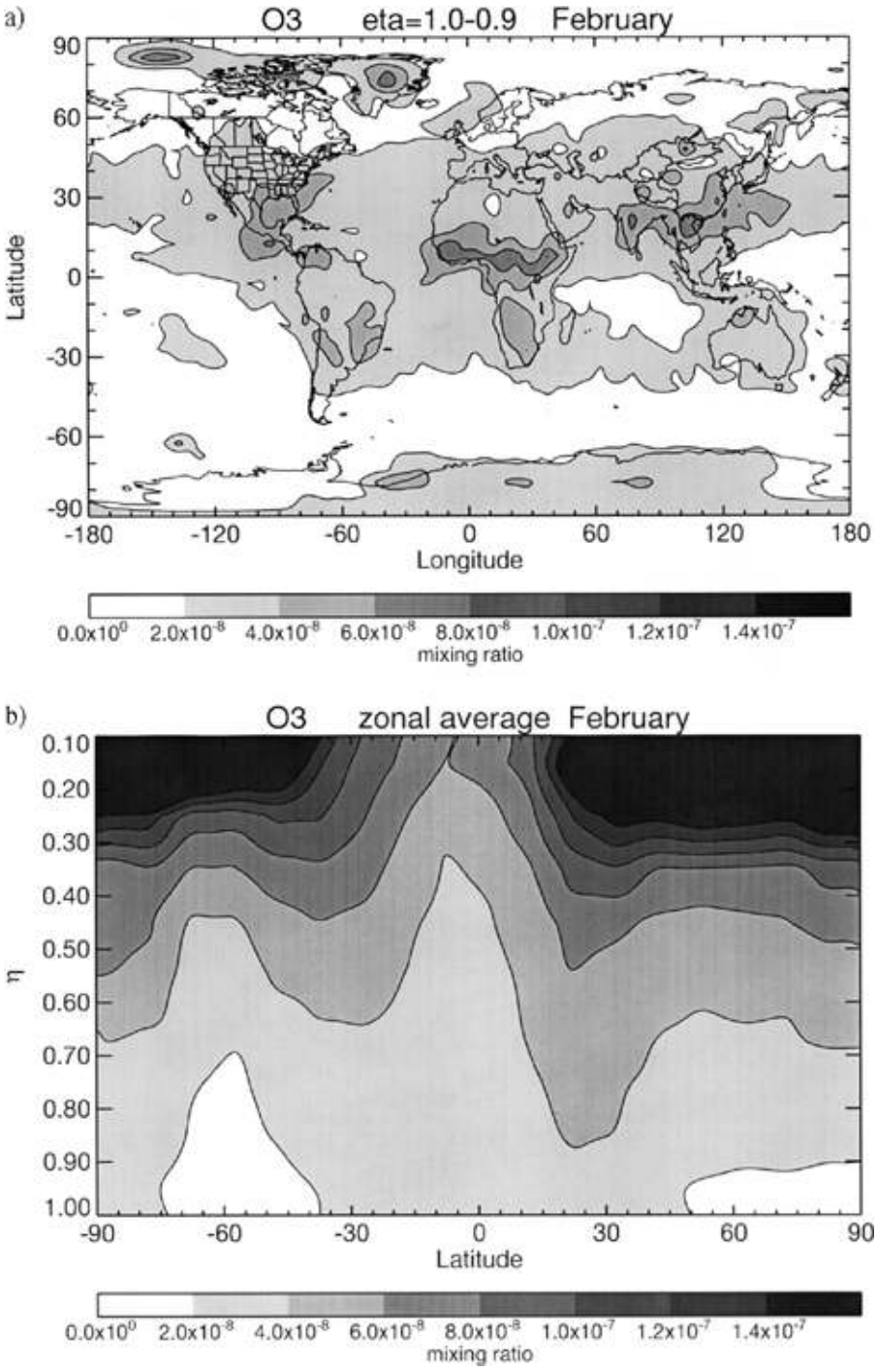
a)
O3 eta=1.0-0.9 February
Latitude
90
60
30
0
-30
-60
-90
-180
-120
-60
0
60
120
180
Longitude
0.0x10^0 2.0x10^-8 4.0x10^-8 6.0x10^-8 8.0x10^-8 1.0x10^-7 1.2x10^-7 1.4x10^-7
mixing ratio
b)
O3 zonal average February
η
0.10
0.20
0.30
0.40
0.50
0.60
0.70
0.80
0.90
1.00
-90
-60
-30
0
30
60
90
Latitude
0.0x10^0 2.0x10^-8 4.0x10^-8 6.0x10^-8 8.0x10^-8 1.0x10^-7 1.2x10^-7 1.4x10^-7
mixing ratio

Figure 2a–2b.

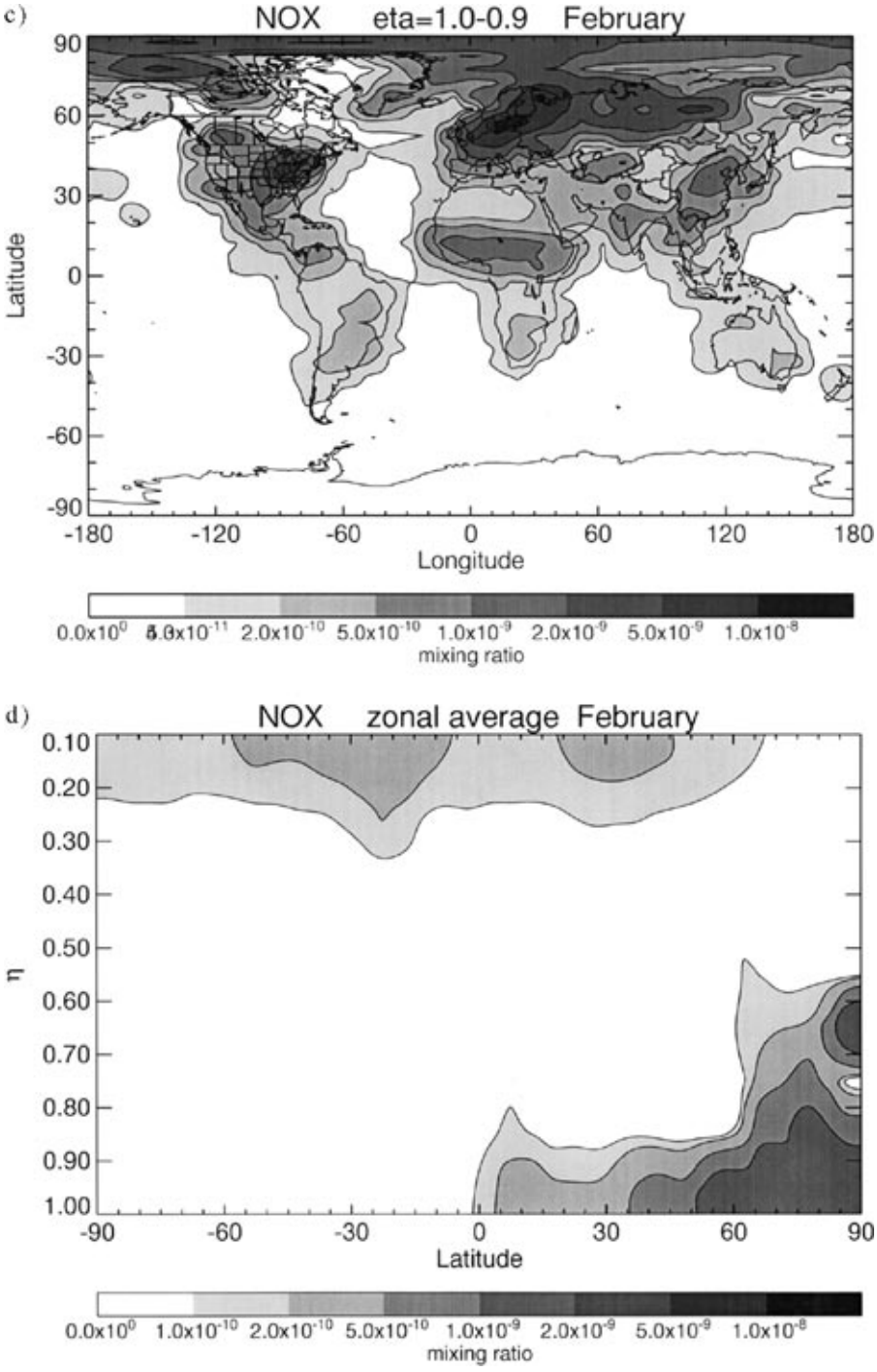
c)
NOX eta=1.0-0.9 February
Latitude
Longitude
mixing ratio
d)
NOX zonal average February
η
Latitude
mixing ratio

Figure 2c–2d.

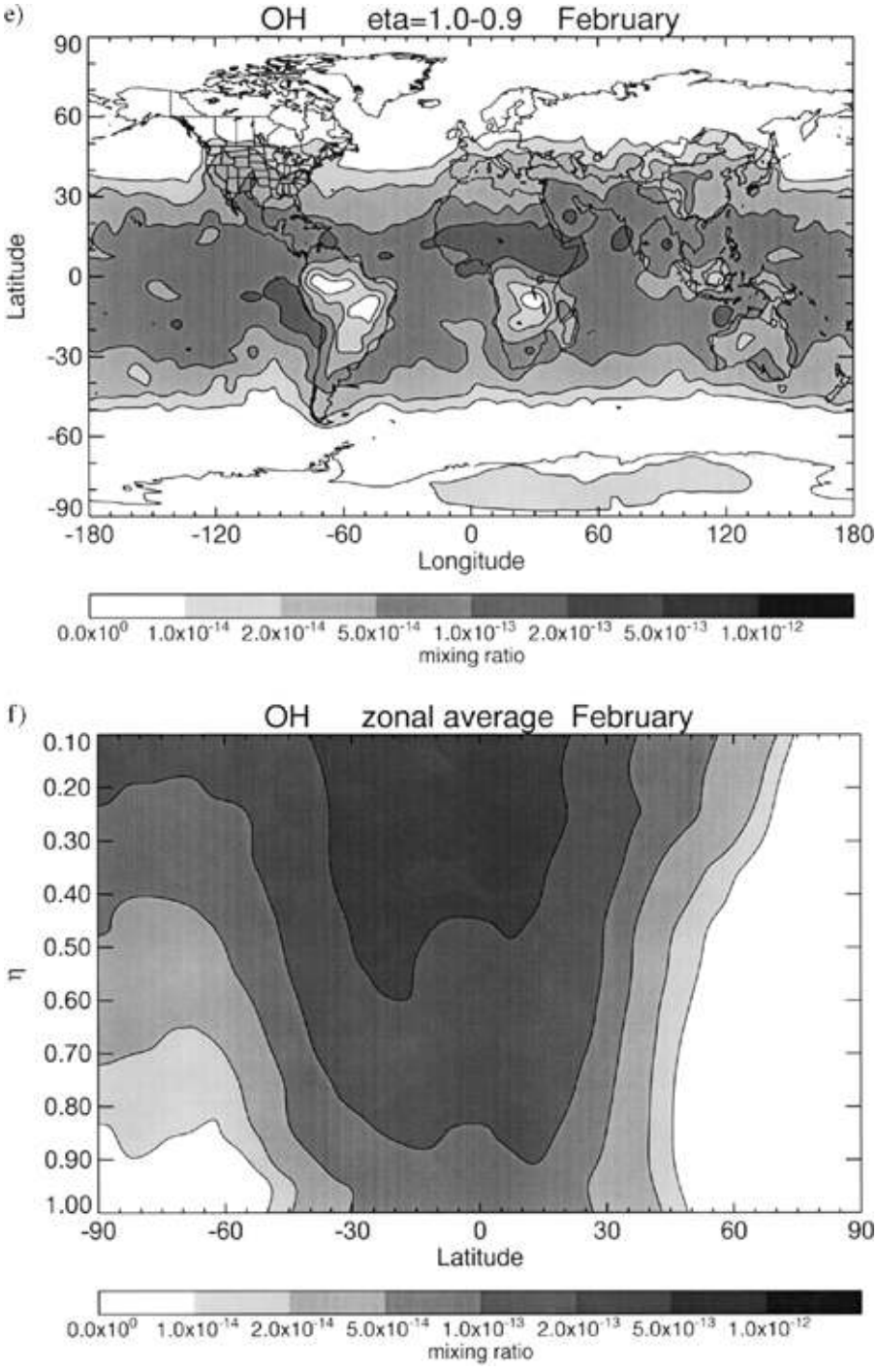
e)
OH eta=1.0-0.9 February
Latitude
Longitude
mixing ratio
f)
OH zonal average February
η
Latitude
mixing ratio

Figure 2e–2f.

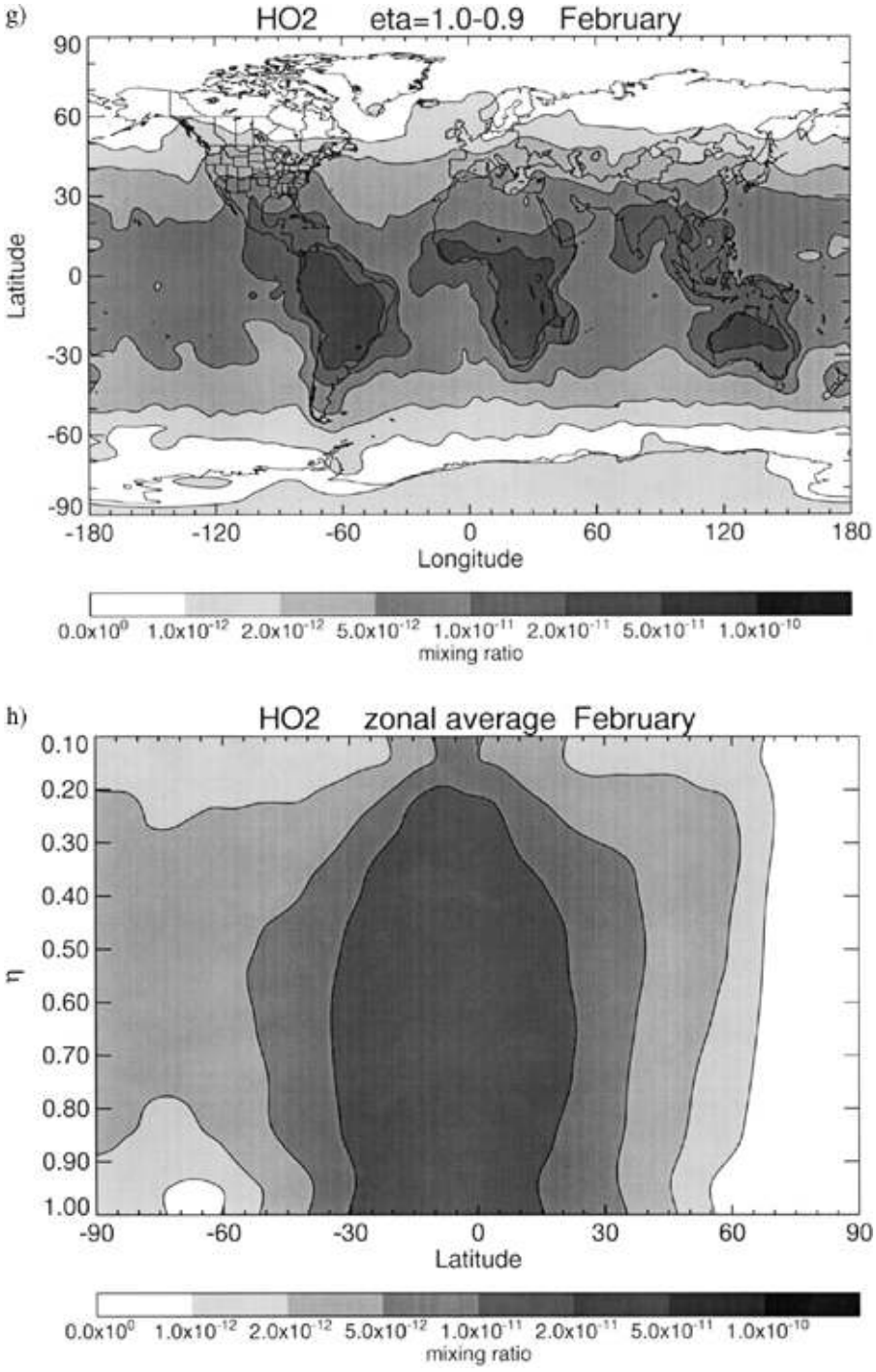

Figure 2g–2h.

Figure 2. Near surface mixing ratios of O_3, NO_X, OH and HO_2 averaged over the 5 days ending on 17th February.

South America, Southern Africa, South East Asia and Australia, whereas the NO_X comes from biomass burning in Central Africa, Central America and China. The spatial variations in the emissions of different species are well resolved in our model. The zonal average profile (Figure 2h) is similar to a mirror image of the August one. The main differences being less HO_2 near the surface and more HO_2 at the top level of the model. The increase at the top level is probably due to the increased downward flux of stratospheric ozone, the decrease at the bottom probably due to less anthropogenic hydrocarbon sources in the Southern hemisphere.

The ozone distribution in February (Figure 2a) is quite different to the equivalent August distribution. there are now ozone minima in the Northern Hemisphere over the industrial regions. At the low OH and HO_2 mixing ratios found in the Northern winter the ozone production slows down and in the continental boundary layer of northern Europe the anthropogenic emissions of NO_X remove more ozone than they produce, through the titration reactions of ozone with NO and NO_2 (reactions 11 and 12 in Table III). In the tropics, the ozone maxima are found at the overlap of the HO_2 and NO_X distributions as both VOCs and NO are needed to form ozone. In the zonal average profile (Figure 2b) the concentrations are lower at the surface in the Northern Hemisphere in February than in August, this is due to the titration effect as explained above. There is however a larger ozone peak at the top of the model in the Southern Hemisphere than there was in August. There is little change in ozone emissions compared to August but in the austral summer the greater actinic flux leads to an increase in HO_2 and NO_X and an increase of ozone production over destruction.

3.3. BUDGETS

To gain a better insight into the factors controlling the photochemistry in the model, it is instructive to look at the fluxes through the important reactions. Tables VII and VIII list the global fluxes that comprise the production and loss terms of NO_Y and O_3, integrated over the five days of 12–17 August and February.

The oxides of nitrogen (NO_Y) can be divided into two groups NO_X (NO + NO_2) and NO_Z (NO_3 + $2N_2O_5$ + HNO_3 + PAN). The largest fluxes for NO_Y are the interconversions $NO_X \rightarrow NO_Z$ and $NO_Z \rightarrow NO_X$ (see Table VII). The net flux is always to convert NO_X to NO_Z and is roughly a tenth of the interconversion rate. The large difference in the interconversion rates between August and February (almost a factor of two) is mostly due to the stability of PAN in the Northern Hemisphere in the winter. The small (about 15%) difference in the net $NO_X \rightarrow NO_Z$ conversion is due to less formation of nitrate aerosol from NO_3 + isoprene in February. We might be slightly over or underestimating the deposition of HNO_3 (and hence the $NO_X \rightarrow NO_Z$ conversion) in the winter since our reaction of N_2O_5 with water to form HNO_3 is in the gas phase rather than on aerosols. There is net NO_Y production in February and almost none in August, this is not a problem with model spin up as the model has spun up for 16 and 10 months, respectively,

Table VII. Reactive nitrogen (NO_Y) budget. Fluxes are global totals for the last five days of the model runs

Reactive nitrogen (NO_Y)	Flux (molecules/5 days)	
	August	February
Production		
Surface emission of NO_X	2.950×10^{34}	2.619×10^{34}
Stratospheric input of NO_Z	1.3×10^{32}	4.7×10^{32}
Total production	2.963×10^{34}	2.666×10^{34}
Interconversions		
$NO_Z \rightarrow NO_X$	4.1955×10^{35}	2.3003×10^{35}
$NO_X \rightarrow NO_Z$	4.4967×10^{35}	2.5670×10^{35}
net $NO_X \rightarrow NO_Z$	3.012×10^{34}	2.667×10^{34}
Removal		
NO_2 deposition	1.00×10^{33}	1.76×10^{33}
HNO_3 deposition	1.884×10^{34}	1.859×10^{34}
PAN deposition	2.82×10^{33}	1.85×10^{33}
Nitrate aerosol formation	6.95×10^{33}	3.30×10^{33}
Total removal	2.961×10^{34}	2.550×10^{34}
Net NO_Y production	2×10^{31}	1.16×10^{33}

whereas NO_Y has a lifetime about 10–15 days in February. As our emissions do not change annually the net NO_Y production averaged over a year will be zero, but February happens to be a time when NO_X emissions are increasing so the NO_Y system is out of chemical equilibrium and there is a net increase in NO_Y over the 5 days in the middle of February.

The global area average net photochemical production of ozone in the summer (August) is 1.2×10^{11} molecules cm^{-2} s^{-1}, this compares with a stratospheric input of 1.8×10^{10} molecules cm^{-2} s^{-1} and dry deposition flux of 1.2×10^{11} molecules cm^{-2} s^{-1}. The fluxes for the winter (February) are 7.2×10^{10}, 6.2×10^{10} and 9.6×10^{10} (all in molecules cm^{-2} s^{-1}) for the net chemical production, stratospheric influx and dry deposition, respectively. If we estimate average annual fluxes by taking the averages of the August and February values then we arrive at fluxes of 1.0×10^{11}, 4.0×10^{10} and 1.0×10^{11} molecules cm^{-2} s^{-1}. By net chemical production we mean the sum of the production fluxes (excluding stratospheric ozone input) minus the sum of the destruction fluxes (excluding ozone dry deposition). The values for production are comparable to Strand and Hov (1994) whereas those for dry deposition are about 50% lower. They give 1.09×10^{11}, 4.1×10^{10} and 1.49×10^{11} molecules cm^{-2} s^{-1} for the chemical production, stratospheric influx and dry deposition respectively.

The total global ozone production can be broken down into the individual production and removal terms as listed in Table VIII. Nearly all the photochemical production of ozone is through the photolysis of NO_2 (Equation (12)) and so it is more useful to look at the production and removal of both O_3 and NO_2. The major production term is the reaction of HO_2 and NO, HO_2 is found over most of the globe in regions of photochemical radical production. Then comes the flux through CH_3O_2 + NO. The sum of the production terms representing the RO_2 + NO reactions of the two isoprene oxidation products $HOC_5H_8O_2$ and $CH_3COCH(O_2)CH_2OH$ is greater than the total of the fluxes through the remainder of the RO_2 + NO reactions. CH_3O_2 is produced by the oxidation of methane throughout the troposphere and over polluted regions by the oxidation of longer chain hydrocarbons. In contrast, the other peroxy radicals tend to be produced over continental areas because they are only produced from nonmethane hydrocarbons. The total photochemical loss for ozone is slightly over three times the dry deposition flux in both August and February. Because we are including NO_2 production/loss as ozone production/loss, reactions NO + NO_3 and NO_3 + $h\nu$ each count as producing two ozone molecules per reaction and NO_2 + O_3 counts as destroying two ozone molecules.

It is interesting to investigate which precursors are producing the peroxy radicals (HO_2 and RO_2) that are so necessary for ozone formation. The most important production and loss terms are listed in Table IX. From this table it appears that the largest peroxy radical production terms are OH attack on CH_4 and CO. This is because the lifetimes of CH_4 and CO are long enough for them to be spread throughout the troposphere to react in the regions where the OH concentration is high, that is away from continental pollution sources. But in these regions the NO_X concentration is so low that the many of the peroxy radicals recombine without producing any ozone. In fact in the ozone producing regions the major source of radicals is from the oxidation and photolysis of HCHO which is derived from CH_3O_2. In the continental boundary layer this comes mostly from the breakdown of non-methane hydrocarbons which we can determine in our model from the three dimensional reaction fluxes. In both August and February, isoprene and its oxidation product methyl vinyl ketone (MVK) provide the largest sources of radicals of those formed from the oxidation of the nonmethane hydrocarbons, although the contribution is less in February. Much of the decrease in peroxy radical production between August and February can be explained by the decrease in isoprene emissions. The major peroxy radical loss in the continental boundary layer is the HO_2 + NO reaction. HO_2 + HO_2 is more significant away from the polluted regions and in the winter.

4. Discussion and Evaluation

Although in a Lagrangian model there is no explicit grid resolution, we have necessarily imposed an artificial resolution. This is most evident for the emission fields; in order to ensure a high probability of finding a cell within the boundary

Table VIII. Major ozone production and removal terms. Fluxes are global totals for the last five days of the model runs

Ozone				
Reaction			Flux (molecules/5 days)	
			August	February
Production				
HO_2+NO	→	OH+NO_2	7.50×10^{35}	6.31×10^{35}
CH_3O_2+NO	→	HO_2+NO_2+HCHO	1.28×10^{35}	1.07×10^{35}
$HOC_5H_8O_2$+NO	→	HO_2+NO_2+products	6.4×10^{34}	5.0×10^{34}
$CH_3COCH(O_2)CH_2OH$+NO	→	HO_2+NO_2+products	6.1×10^{34}	4.6×10^{34}
RO_2+NO	→	HO_2+NO_2+products	9.1×10^{34}	6.2×10^{34}
NO+NO_3	→	2NO_2	6×10^{33}	4×10^{33}
NO_3+$h\nu$	→	NO_2+O(^{3}P)	2.0×10^{34}	1.3×10^{34}
Stratospheric influx			4.0×10^{34}	1.36×10^{35}
Total production			1.186×10^{36}	1.066×10^{36}
Removal				
O_3+$h\nu$+H_2O	→	2OH	2.74×10^{35}	3.02×10^{35}
O_3+HO_2	→	OH+2O_2	3.77×10^{35}	2.93×10^{35}
O_3+OH	→	HO_2	1.64×10^{35}	1.28×10^{35}
O_3+NO_2	→	NO_3+O_2	3.2×10^{34}	2.0×10^{34}
O_3+olefins	→		6×10^{33}	5×10^{33}
O_3 dry deposition			2.59×10^{35}	2.12×10^{35}
NO_2 dry deposition			1×10^{33}	2×10^{33}
PAN dry deposition			3×10^{33}	2×10^{33}
Total removal			1.148×10^{36}	9.84×10^{35}
Production-Removal			3.8×10^{34}	8.2×10^{34}

layer over an emission site the sites have to be sufficiently large. For convenience we chose $5^\circ\times5^\circ$, this is far too large to be able to distinguish between rural and urban areas, the area of each square is of the order of a small European country. Therefore our chemistry will in some sense be an average of the conditions in urban, rural and remote areas which makes it difficult to make comparisons with data except in regions where there is little spatial variation in emissions.

Another factor that will influence the chemistry is the time resolution of the meteorology. For a description of the evaluation of the transport processes in our model, see Stevenson *et al.* (1997a). At present we use 18-day averages for the wind, temperature, cloud and boundary layer fields. This does not fully resolve individual weather systems such as depression tracks which will readily mix the pollutants throughout the depth of the troposphere, or high pressure systems which concentrate pollutants and lead to elevated ozone episodes. At the current model resolution the aim is to model the average monthly chemistry over a large geographical region.

Table IX. HO_2 and RO_2 production terms. Fluxes are global totals for the last five days of the model runs

RO_2 production		
	Flux (molecules/5 days)	
	August	February
Reactions with OH		
H_2	9.3×10^{34}	8.9×10^{34}
H_2O_2	1.89×10^{35}	2.07×10^{35}
O_3	1.64×10^{35}	1.27×10^{35}
CO	9.70×10^{35}	9.56×10^{35}
CH_4	2.87×10^{35}	2.64×10^{35}
C_2H_6	5×10^{33}	5×10^{33}
n-C_4H_{10}	9×10^{33}	9×10^{33}
C_2H_4	1.6×10^{34}	1.2×10^{34}
C_3H_6	8×10^{33}	6×10^{33}
C_5H_8	6.8×10^{34}	5.5×10^{34}
toluene	1×10^{33}	1×10^{33}
HCHO	1.76×10^{35}	1.46×10^{35}
CH_3CHO	1.3×10^{34}	1.1×10^{34}
$CH_3COC_2H_5$	9×10^{33}	9×10^{33}
methyl maleic dialdehyde	2×10^{33}	2×10^{33}
methyl vinyl ketone	6.9×10^{34}	5.4×10^{34}
Total OH $\rightarrow$ RO_2	2.079×10^{36}	1.953×10^{36}
Reactions with NO_3		
C_5H_8	7×10^{33}	3×10^{33}
others	3×10^{33}	2×10^{33}
Total NO_3 $\rightarrow$ RO_2	1.0×10^{34}	5×10^{33}
Photolysis		
(2$\times$) methyl glyoxal	1.05×10^{35}	8.5×10^{34}
(2$\times$) HCHO	1.30×10^{35}	1.13×10^{35}
(2$\times$) CH_3CHO	1×10^{33}	1×10^{33}
(2$\times$) $CH_3COCOCH_3$	9×10^{33}	9×10^{33}
CH_3O_2H	1.66×10^{35}	1.55×10^{35}
Total photolysis	8.56×10^{35}	5.72
Total production	2.745×10^{36}	2.530×10^{36}
Loss		
HO_2+O_3	3.77×10^{35}	2.93×10^{35}
HO_2+NO	7.50×10^{35}	6.31×10^{35}
HO_2+OH	1.55×10^{35}	1.56×10^{35}
(2$\times$) HO_2+HO_2	5.08×10^{35}	5.21×10^{35}
(2$\times$) HO_2+CH_3O_2	2.03×10^{35}	1.88×10^{35}
(2$\times$) CH_3O_2+CH_3O_2	2×10^{33}	1×10^{33}
(2$\times$) CH_3O_2+CH_3COO_2	1.7×10^{34}	1.5×10^{34}
Total loss	2.742×10^{36}	2.530×10^{36}

4.1. COMPARISON OF OH CONCENTRATIONS WITH OBSERVATIONS

The global mean OH concentration in our model is 14.1×10^5 molecules cm^{-3} in August and 13.9×10^5 molecules cm^{-3} in February averaged over the entire model domain, pole-to-pole and 0–16 km. Estimates of the global OH concentration have been made by measurements of the lifetime of methyl chloroform in the troposphere. Prinn *et al.* (1995) calculated a mean tropospheric OH concentration of $9.7\pm0.6\times10^5$ molecules cm^{-3}. This is not, however, a straightforward volume average but is weighted by the methyl chloroform concentration, in the same paper the calculated OH distribution was used to calculate methane lifetimes of 8.0 ± 0.5 years between 1000 and 200 hPa and 8.9 ± 0.6 years between 1000 and 0 hPa. The above calculations did not take into account the seasonal cycle of OH. The methane lifetimes in our model between 1000 and 100 hPa are 7.9 and 8.4 years in August and February, respectively. Our numbers agree to well within the scope of the errors.

4.2. COMPARISON OF O_3 CONCENTRATIONS WITH OBSERVATIONS

Surface ozone concentrations within the boundary layer tend to be measured a few tens of metres from the ground. This poses a problem for comparisons with our model since, to include enough Lagrangian cells to get a sufficiently accurate horizontal resolution, we average the species mixing ratios over the range η = 1.0–0.9 (surface to $\sim$1.0 km). Over the continents, nighttime ozone measurements will be characteristic of the ozone-depleted shallow nocturnal boundary layer (height $<$ 0.3 km) whereas the near-surface ozone concentrations in our model will include a large contribution from the free troposphere. Hence, the model concentrations will be higher than the diurnal average of the observed concentrations but lower than the daytime values.

Oceanic measurements of ozone will not have the problem with the nocturnal boundary layer and so should agree with the model results. Results from Winkler (1988) for the Atlantic Ocean in Figures 3a and b show good agreement with our model in the more remote regions but we allow too much ozone to spread over the Atlantic from continental high ozone producing areas.

We have compared ozonesonde data (Komhyr *et al.*, 1989) with our model in Figures 5a and b. Resolute, Barrow and Lauder show good agreement, the others less so. The profiles for Edmonton and Boulder are more vertical than the observed data, overpredicting in the lower troposphere and underpredicting in the upper troposphere, this could possibly be due to convection bringing down too much ozone from aloft. Our convective mass fluxes (although diurnally varying) are 18 day averages rather than individual events. All the winter profiles show good agreement between the model and the data.

A series of ozone measurements from various sites (Oltmans and Levy, 1994; Combrink *et al.*, 1995; Derwent *et al.*, 1994; Gregory *et al.*, 1988; Poulida *et al.*, 1991) are shown in Figures 4a and b. Many of the observations show good

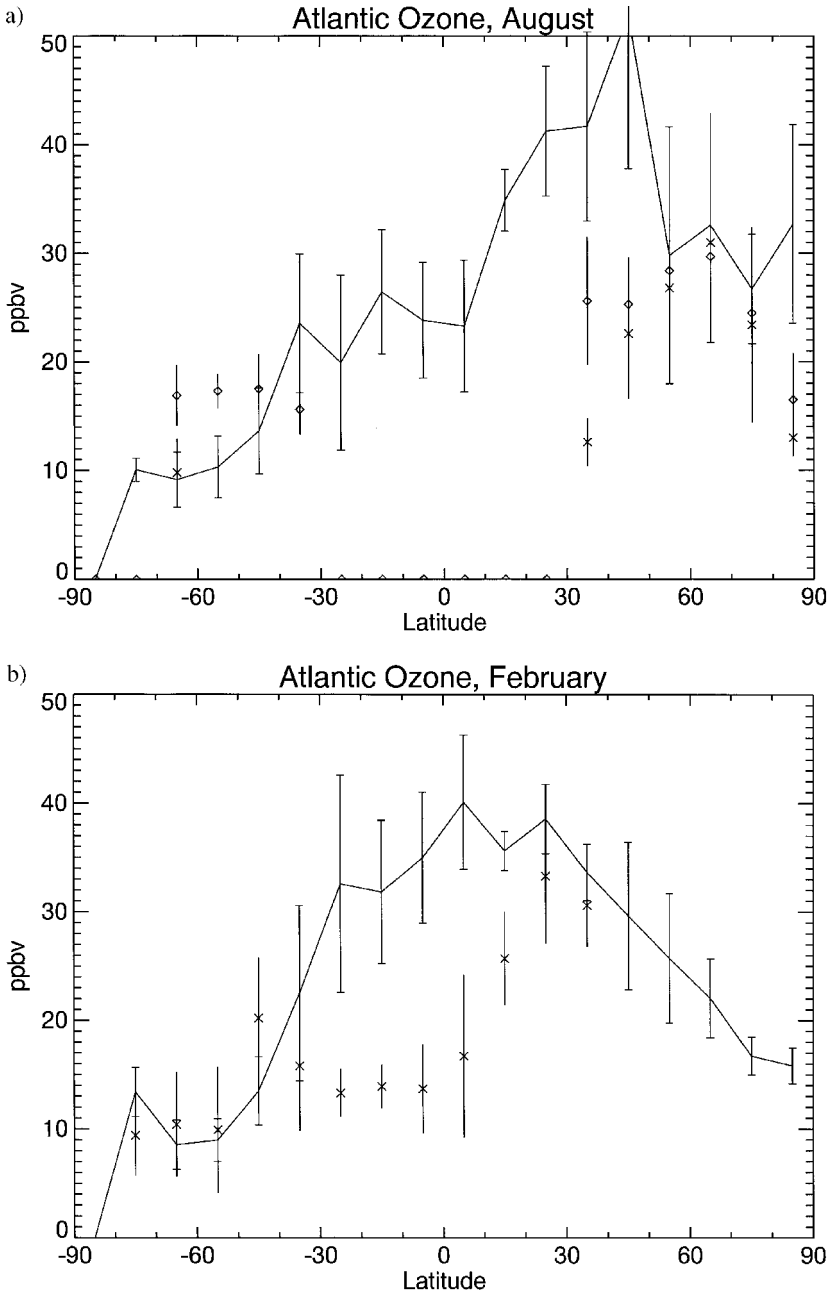

Figure 3. Comparison of surface ozone measurements with model calculations for the Atlantic for August (a) and February (b). The crosses are observations and the continuous line the model data. In (a) additional observations for July have been plotted as diamonds as there were fewer data for August. Observations are taken from Winkler (1988). The model data were averaged over latitude bands covering the area of the observations and the ranges for the model results represent the standard deviation of the model concentrations over the latitude bands.

agreement with the model in August. Notable exceptions are Bermuda, Amazonia and Virginia. Bermuda is affected by the advection in our model of ozone and ozone precursors out from the United States, Virginia and Amazonia are in areas of high ozone production in our model which are due to anthropogenic and biogenic emissions respectively. In February we underpredict the ozone at both Barrow and Reykjavik which may be due to simulating a slower downward transport of ozone than actually occurs. We predict more ozone production in South Africa in February than is observed.

4.3. COMPARISON OF NO_X CONCENTRATIONS WITH OBSERVATIONS

Measurements of NO_X areas have been reviewed by Carroll *et al.* (1992) and are shown in Figure 6 along with surface winter NO_X data from Harvard Forest (Munger *et al.*, 1996) and winter NO_2 EMEP data (Hjellbrekke *et al.*, 1996). The model results agree very well with all the measurements. A two-dimensional (latitude altitude) cross section of NO_X measurements from the STRATOZ III campaign has been compiled by Ehhalt and Drummond (1988) and comparison between this and a cross section over a similar region from our model is shown in Figure 7. The agreement is particularly good in the top half of the troposphere. Below $\eta = 0.7$ the STRATOZ measurements see a lot of continental NO_X whereas model values are all taken from over the ocean. The very good agreement between our NO_X concentrations and measured values encourages us to believe that our NO_X chemistry is a good approximation to reality even in the winter boundary layer.

5. European NO_X Control and Its Impacts on Tropospheric Chemistry

In order to provide a test for our model, we investigated the effect of an emission control scenario on the model ozone distribution. This scenario was simply a cut in anthropogenic NO_X emissions over Europe by half. The area of Europe was arbitrarily defined as a rectangle bounded in the north and south by the 75°N and 30°N latitude circles, in the west by the 20°W meridian and in the east by the 30°E meridian. The anthropogenic NO_X sources in the 'European' region average 2.2×10^{10} molecules cm^{-2} s^{-1}, with a total mass of 5.2 Tg (N) yr^{-1} out of a global total of 21 Tg (N) yr^{-1}. The reduction scenario is therefore a cut of 2.6 Tg (N) yr^{-1} or 0.007 Tg (N) day^{-1}. This is not necessarily expected to be a realistic scenario but is useful in testing the model. In practice hydrocarbon emissions would also reduce as most anthropogenic NO_X sources are also sources of hydrocarbons.

Two emission control simulations were run, the first for three and a half months from 1 May to 17 August, and the other for three months from 17 November to 17 February. For the purposes of the analyses, the species concentrations were averaged over the last five days of each run.

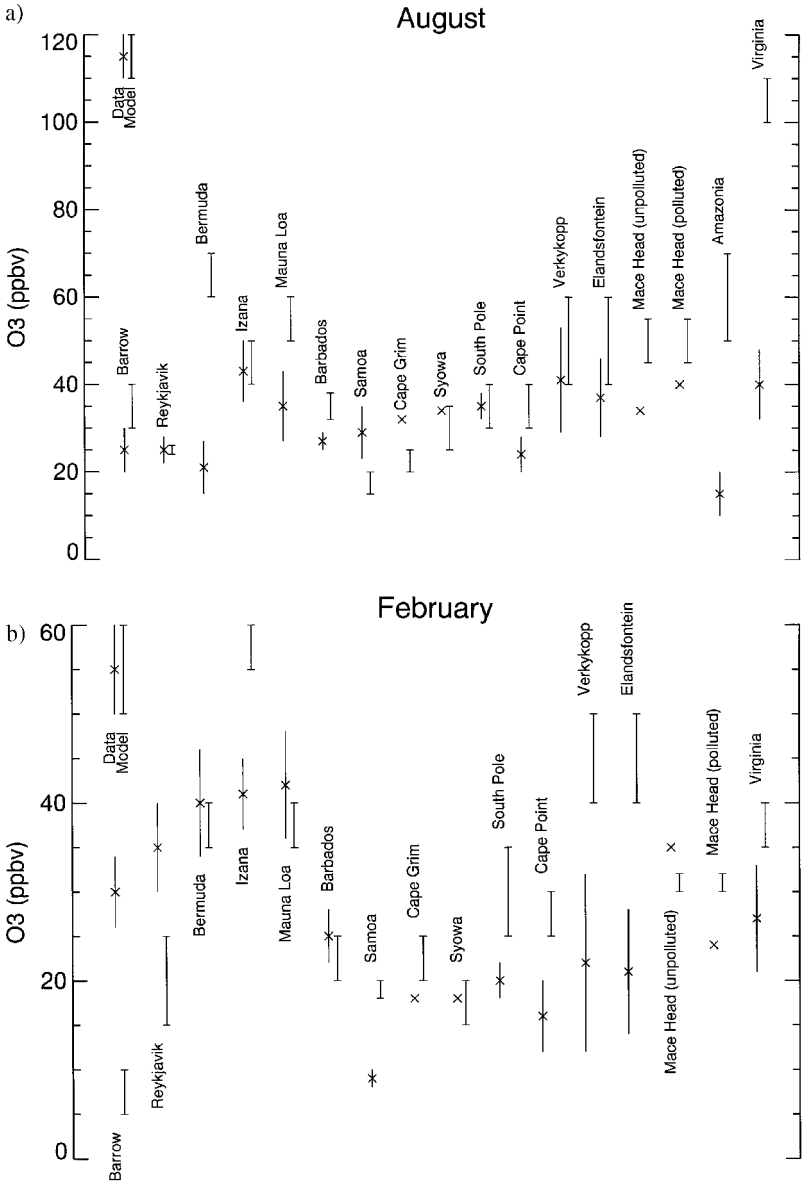

Figure 4. Comparison of ozone measurements with model calculations for August (a) and February (b). Values are all ozone mixing ratios in ppb, the data are crosses, the model values are straight lines with bars at the ends. Observations from Barrow, Reykjavik, Bermuda, Izaña, Mauna Loa, Barbados, Samoa, Cape Grim, Syowa and the South Pole are taken from Oltmans and Levy (1994). The data from Cape Point and Elandsfontein are from Combrink *et al.* (1995). Data from Mace Head are from Derwent *et al.* (1994), those from Amazonia from Gregory *et al.* (1988), and from Virginia from Poulida *et al.* (1991). All data have been estimated from the published graphs rather than tables of values. Where errors are shown, these encompass 50% of the data (25th–75th percentiles). The ranges for the model results reflect the spatial resolution in the output and do not represent any detailed error analysis.

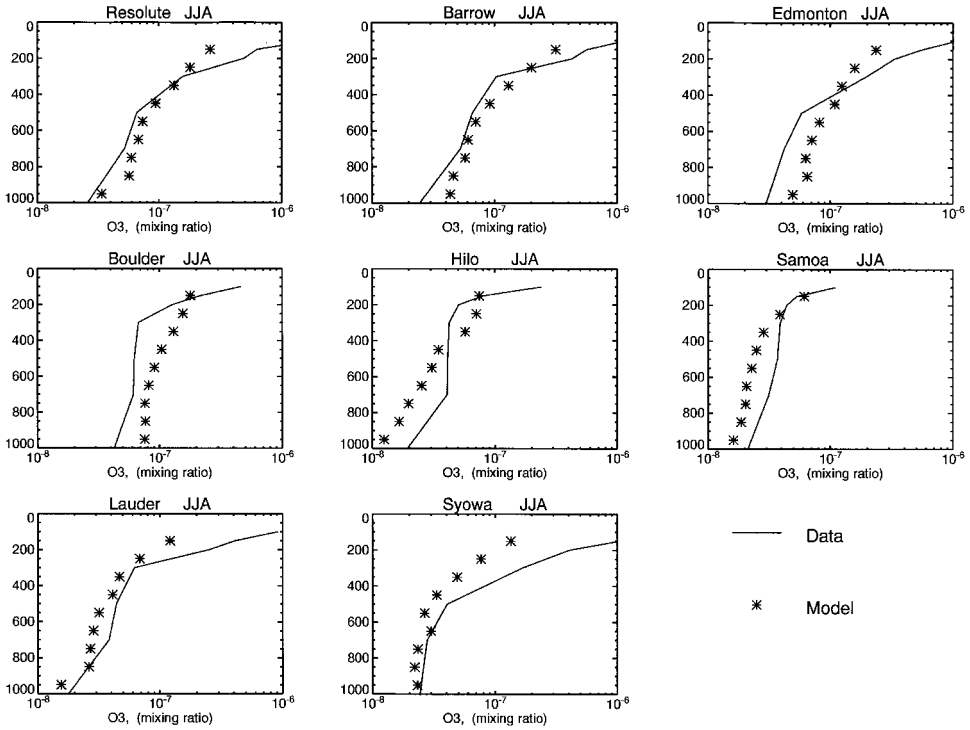

Figure 5a.

5.1. SUMMERTIME CONDITIONS

After the NO_X control, the total model inventory of NO_X decreases by 0.002 Tg and of ozone by 1.2 Tg. This gives a molecular ratio of a decrease of 160 molecules of ozone per molecule reduction in NO_X. The decrease in the NO_X inventory gives a NO_X lifetime in the model of about 6 hours. Figures 8a and b show the fractional decrease in ozone by reducing the NO emissions as a surface plot and as a section from the surface to the top of the model at 10°–15° E. At the surface there is a net reduction in ozone of between 10 and 20% over Europe and a small reduction outside Europe. The section shows that the ozone decrease extends up to $\eta \sim 0.7$ over Europe. A similar experiment by McKeen *et al.* (1991) for the eastern United States gave an average ozone decrease of 12–16% for a halving of the anthropogenic NO_X emissions, in good agreement with our results.

To quantify this more precisely it is instructive to look at the number of ozone molecules reduced per molecule reduction in NO_X. Figures 9a and b show a surface map and a cross-section of the ratio of the change in ozone to that in NO_X. Areas where the change in the NO_X mixing ratio has changed by less than 1 ppt are left blank since there the changes in ozone and NO_X are so tiny that the signal is swamped by noise. At the surface in the polluted regions over Europe the ratio

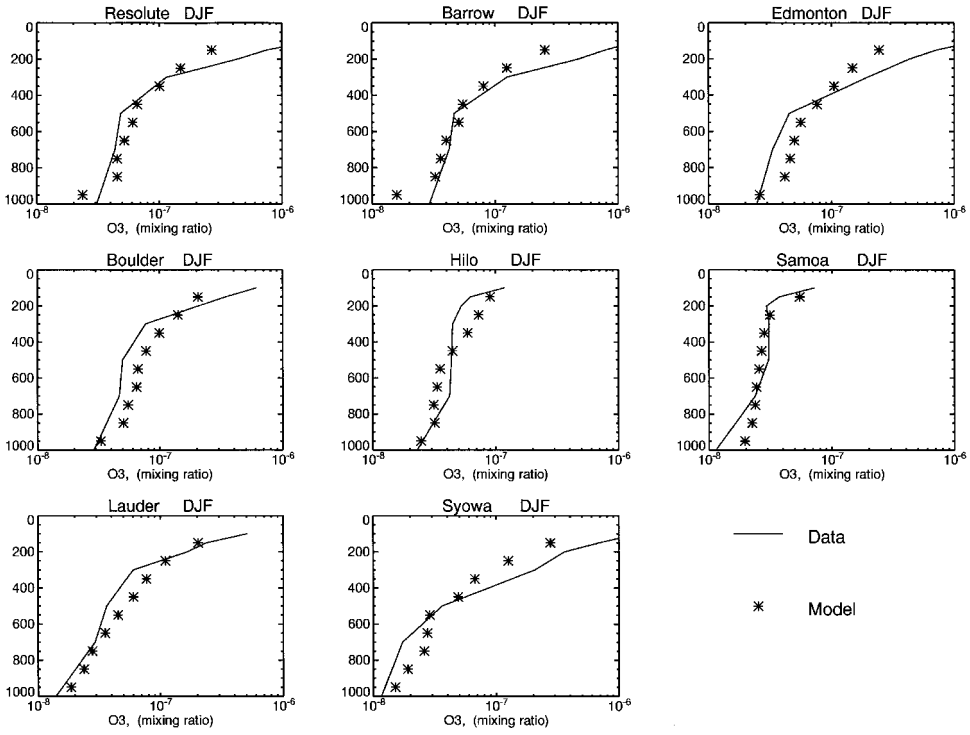

Figure 5b.

Figure 5. Comparison of ozone profile measurements with model calculations for Summer (a) and Winter (b). Values are all ozone mixing ratios, both measurements and observations are averaged over three months (June, July, August for the summer, and December, January, February for the winter). The data are crosses and the model results connected by straight lines. The data are taken from Komhyr *et al.* (1989).

ranges from about 5 to 50. This is larger than in results from Olszyna *et al.* (1994) and Trainer *et al.* (1993) who calculated ratios of 12 and 8.5, respectively, for rural areas of the United States. In the most remote regions the ratio in our model may be artificially increased by ozone transport. From Figure 9b it can be seen that the ratio drops again in the higher NO_X concentrations brought down from the stratosphere. What we see is that the $d[O_3]/d[NO_X]$ ratio is inversely dependent on the NO_X concentration. This is because the main removal process for NO_X is OH + $NO_2 \rightarrow HNO_3$. In regions of low NO_X concentrations most of the odd hydrogen is present as HO_2, but increasing the NO_X concentration alters the odd hydrogen balance towards OH, hence increasing the NO_X concentration increases its own sink and decreases its efficiency to produce ozone. The OH + NO_2 loss process does not remove ozone, it just reduces the efficiency of NO_X to produce ozone.

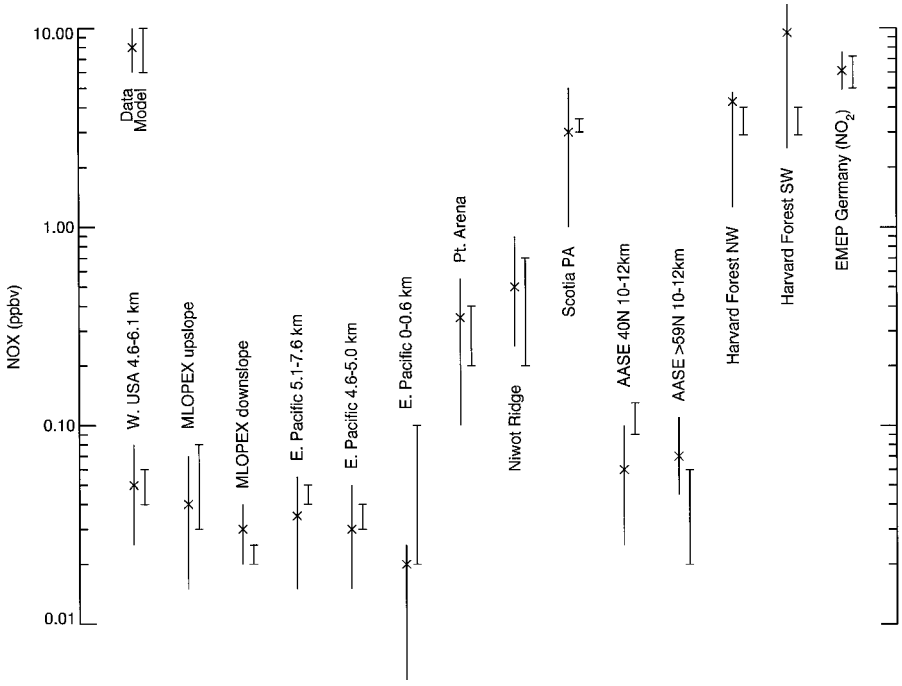

Figure 6. Comparison of NO_X measurements with model calculations. Values are all NO_X mixing ratios in ppb. Most observations are taken from Carroll *et al.* (1992) and have been estimated from the published graph rather than tables of values. Values for Harvard Forest are taken from Munger *et al.* (1996) for two different wind directions NW and SW. We have taken an average of winter surface values over Germany using data from Hjellbrekke *et al.* (1996), these values are only available for NO_2 so have been compared with our model NO_2 values. Errors encompass 50% of the data (25th–75th percentiles). The ranges for the model results reflect the spatial resolution in the output and do not represent any detailed error analysis. The AASE (Airborne Arctic Stratospheric Expedition), Harvard Forest and EMEP Germany data were measured in the winter and are compared with the February model output, all the other data are for spring and summer and are compared with the August model output.

Graphs of the ozone production efficiency against the mixing ratios of NO_X and OH are shown in Figures 10a and b. Each point on the graph represents one grid volume in the model output, and points are coded by symbol according to the CO mixing ratio in each grid volume. Only those grid volumes where the NO_X mixing ratio has changed by more than 10 ppt are used (the looser cut on 1 ppt used in Figures 9a and b was chosen to allow a better visualisation of the geographical variation of the efficiency). These graphs show a negative dependence on the NO_X mixing ratio. Between $[NO_X]$ = 1 ppb and $[NO_X]$ = 10 ppb the efficiency drops by a factor of 10–20 which is roughly in agreement with the results from Lin *et al.* (1988) after they have included the effects of nightime removal of NO_3. This suggests that nighttime chemistry is important over industrial continental regions. Although the efficiency is inversely dependent on the NO_X concentration all the values are still positive which implies that the whole region is in a NO_X-limited

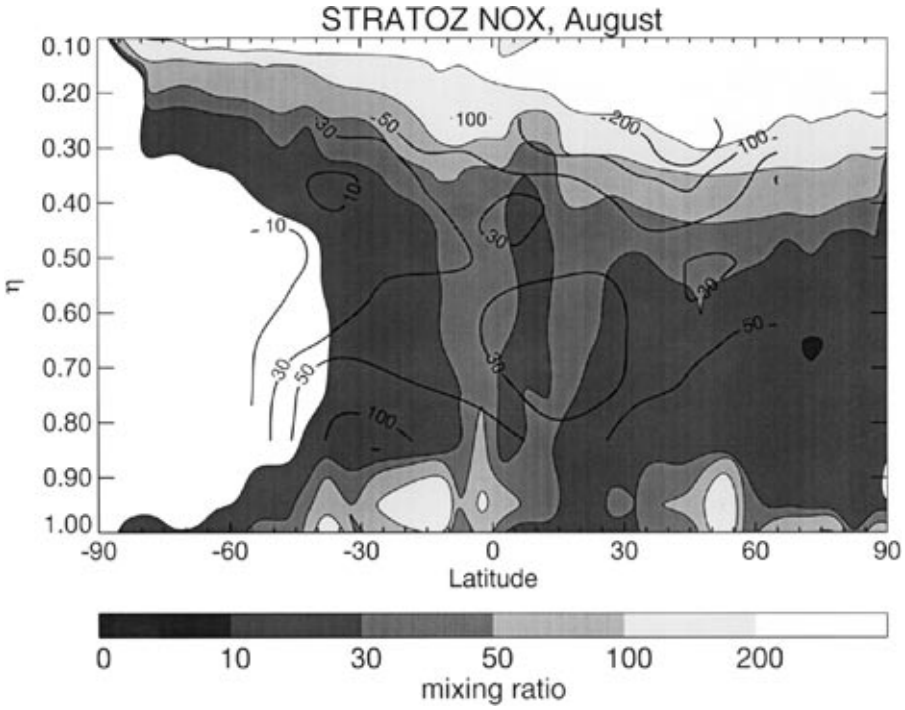

Figure 7. Comparison of STRATOZ III NO_X measurements with model calculations. Values are all NO_X mixing ratios in ppt. The cross section for the data is shown as thick contours and is taken from Ehhalt and Drummond (1988). The model results are the shaded contours and are zonal averages over a similar region to the STRATOZ III flights.

regime even for NO_X levels as high as 10 ppb. This is probably not entirely realistic as ozone production in urban centres is often not NO_X-limited, however our $5^\circ \times 5^\circ$ emission grid is too coarse to resolve these centres and will lead to an overestimate of the total ozone production (Sillman *et al.*, 1990). Simpson (1992b) and (1993) calculated a decrease in mean ozone over Europe in August of 9% after a 50% NO_X reduction (compared with our values of 10–20%), all points showed a reduction in the monthly mean ozone concentrations but a few showed an increase in the maximum August ozone concentrations. For the same NO_X concentration there is still some variation in ozone production efficiency, where those with higher efficiency tend to have higher CO mixing ratios. The presence of hydrocarbons and CO tilts the OH–HO_2 balance away from OH (which is a NO_X sink) and increases the ozone production efficiency.

There is no dependence of the ozone production efficiency on OH mixing ratio (Figure 10b) which suggests that in the European boundary layer the reaction chain is not affected significantly by changes in the OH mixing ratio over an order of magnitude.

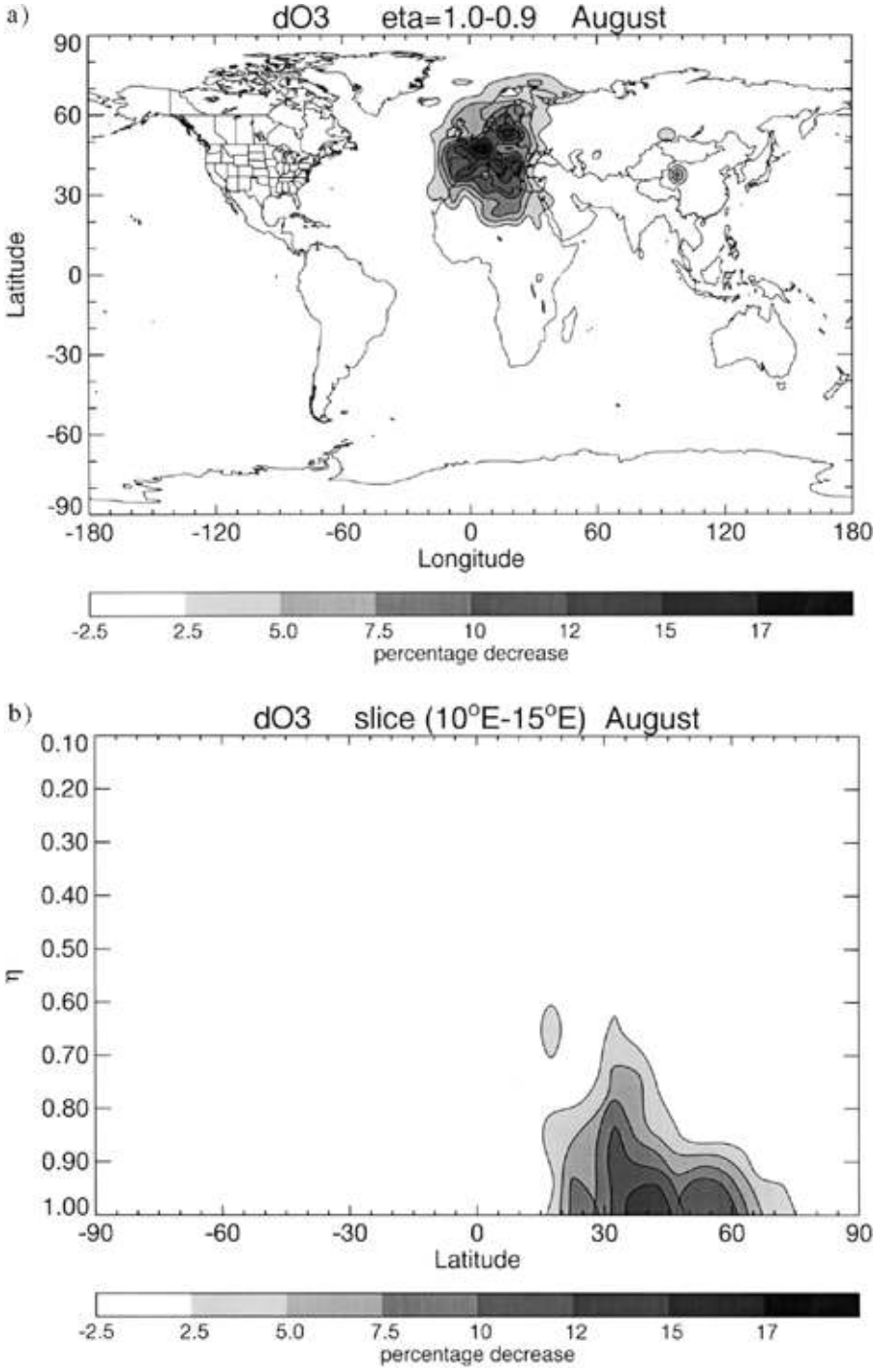
a)
dO3 eta=1.0-0.9 August
Latitude
Longitude
90
60
30
0
-30
-60
-90
-180
-120
-60
0
60
120
180
-2.5
2.5
5.0
7.5
10
12
15
17
percentage decrease
b)
dO3 slice (10°E-15°E) August
η
0.10
0.20
0.30
0.40
0.50
0.60
0.70
0.80
0.90
1.00
-90
-60
-30
0
30
60
90
Latitude
-2.5
2.5
5.0
7.5
10
12
15
17
percentage decrease

Figure 8a–8b.

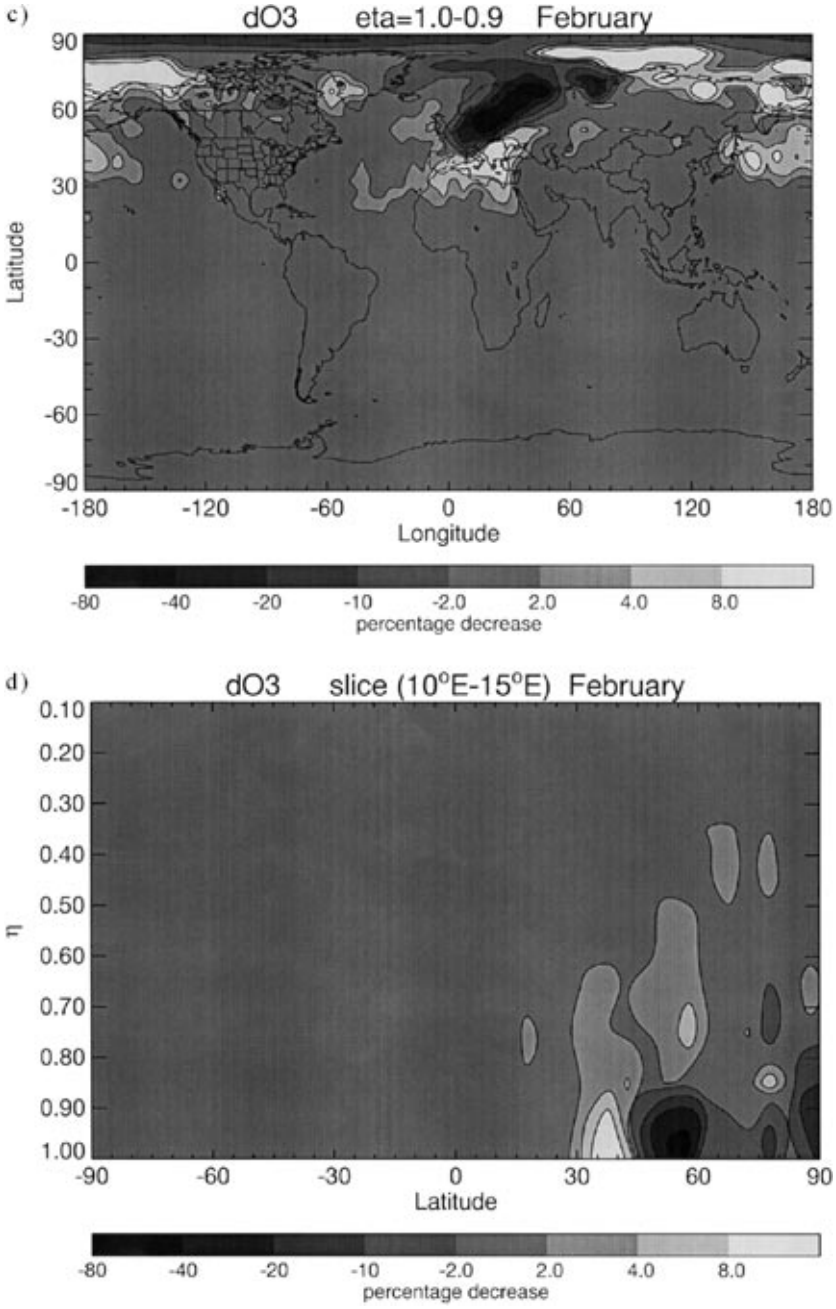

Figure 8c–8d.

Figure 8. Fractional decrease in ozone mixing ratio, using a reduced European NO emission scenario compared with the same run using full NO emissions: (a) surface, August; (b) section, August; (c) surface, February; (d) section, February.

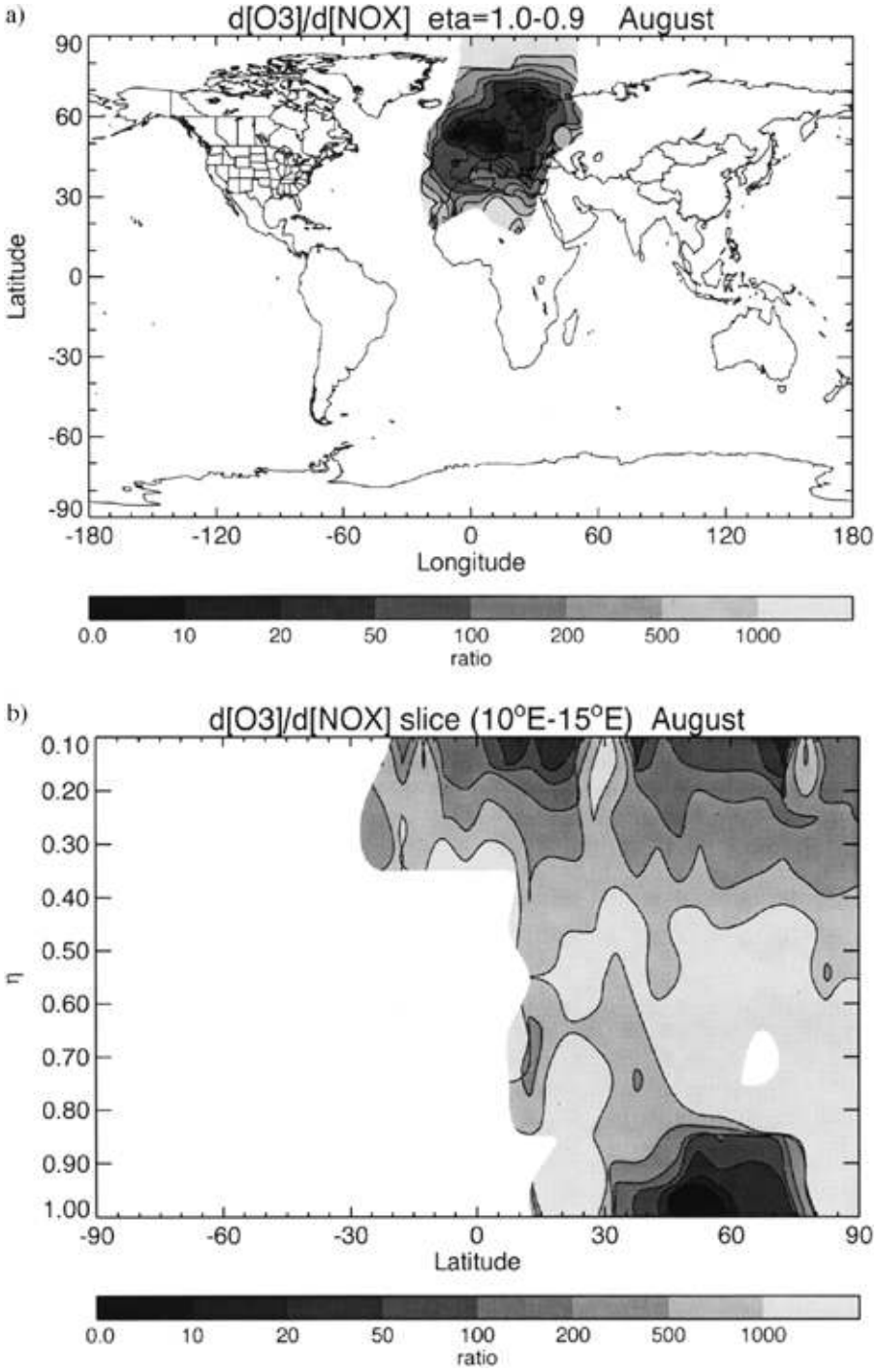
a)
d[O3]/d[NOX] eta=1.0-0.9 August
Latitude
90
60
30
0
-30
-60
-90
-180
-120
-60
0
60
120
180
Longitude
0.0
10
20
50
100
200
500
1000
ratio
b)
d[O3]/d[NOX] slice (10°E-15°E) August
η
0.10
0.20
0.30
0.40
0.50
0.60
0.70
0.80
0.90
1.00
-90
-60
-30
0
30
60
90
Latitude
0.0
10
20
50
100
200
500
1000
ratio

Figure 9a–9b.

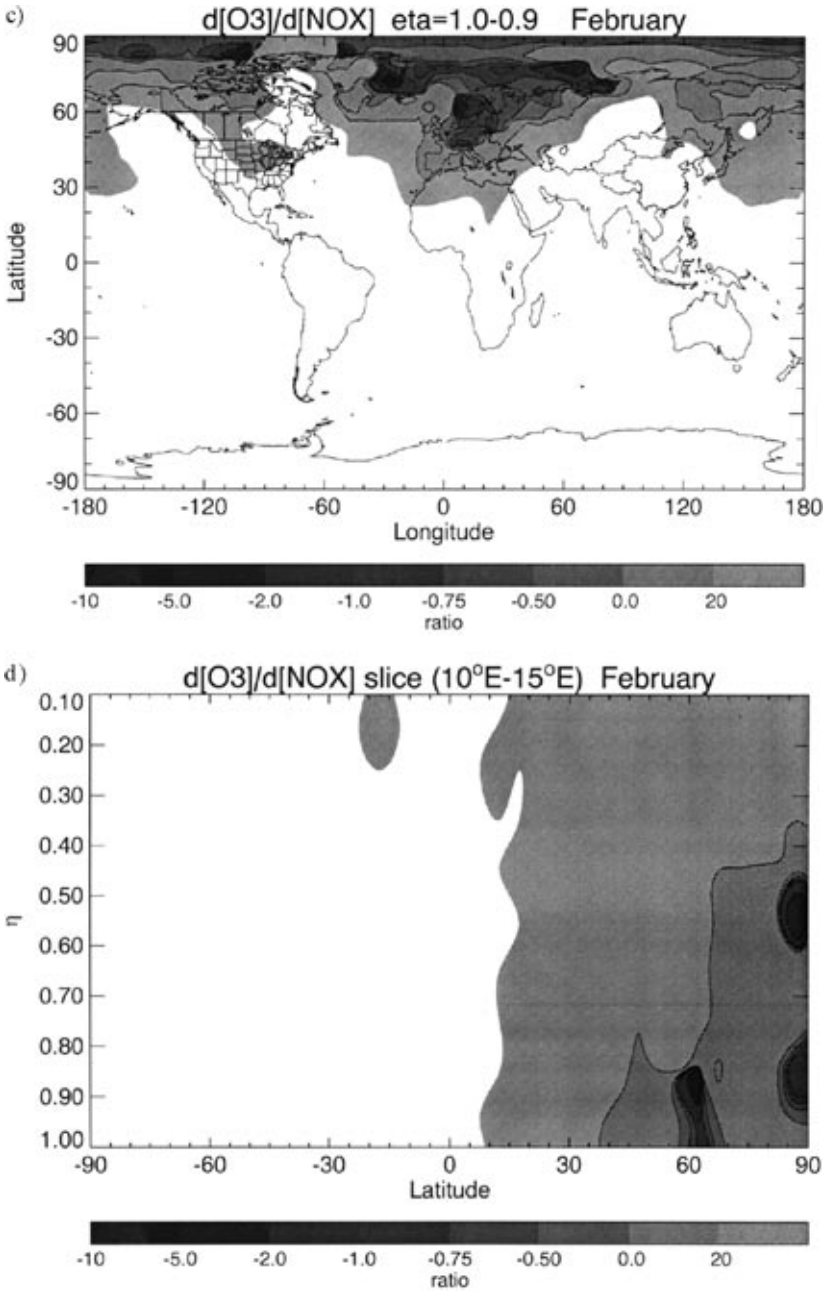

Figure 9c–9d.

Figure 9. Change in ozone mixing ratio divided by the change in NO_X mixing ratio, between the two runs with different NO emission scenarios: (a) surface, August; (b) section, August; (c) surface, February; (d) section, February. Only values where the NO_X mixing ratio has changed by more than 1 part per trillion (1 ppt) are used.

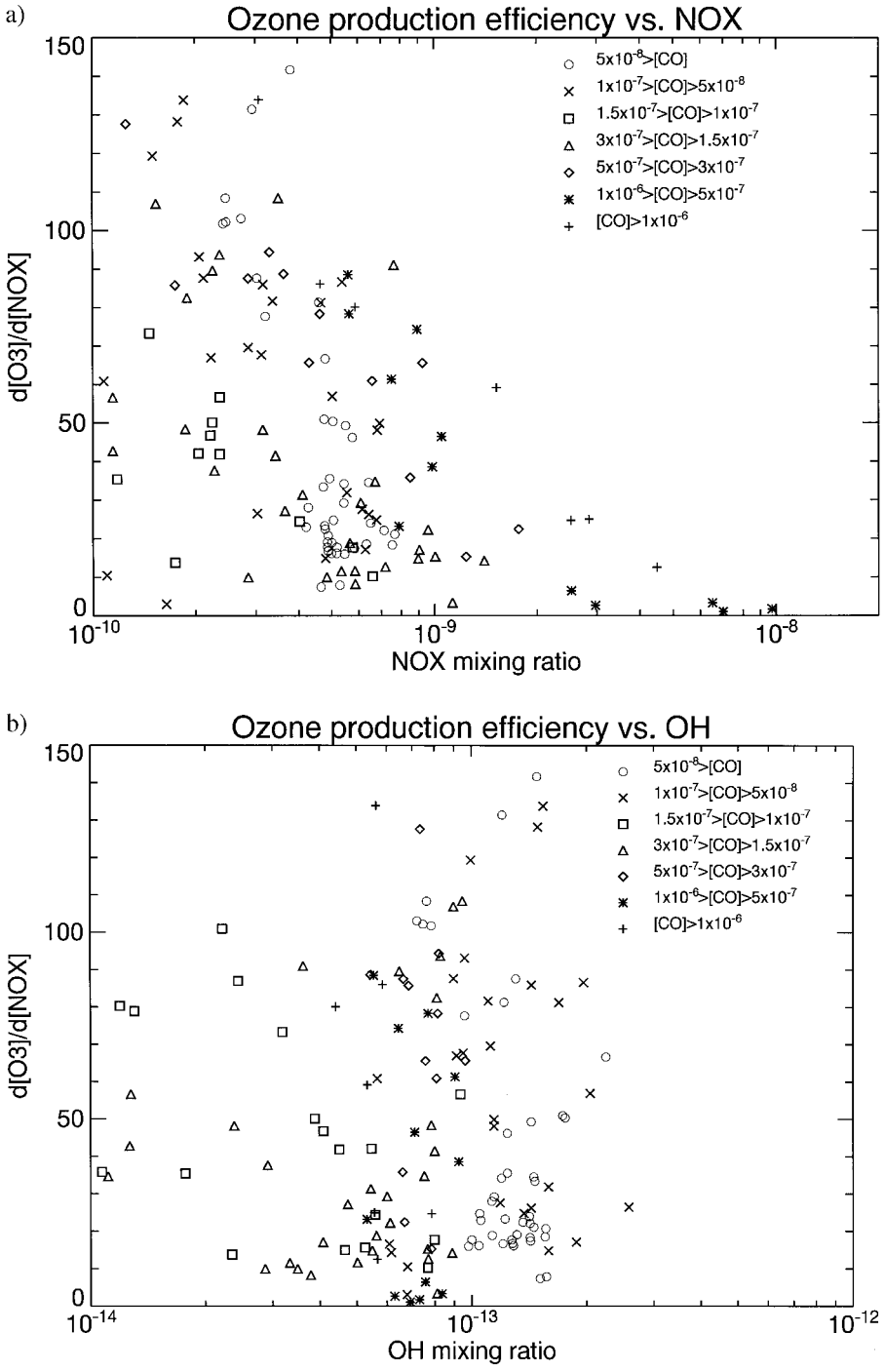

Figure 10a–10b.

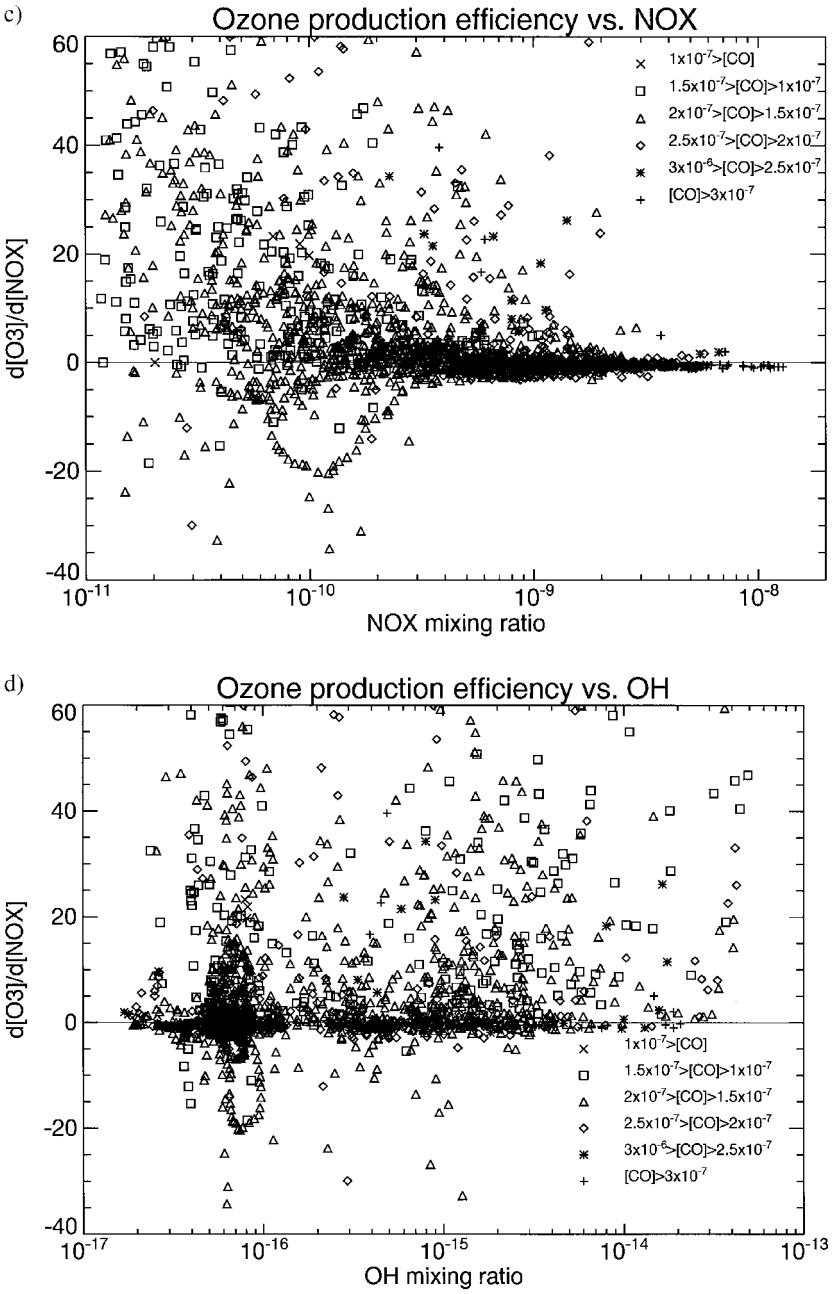

Figure 10c–10d.

Figure 10. Ozone production efficiency, defined as the change in ozone divided by the change in NO_X between the two runs, against the NO_X and OH mixing ratios without emission controls: (a) and (b) August; (c) and (d) February. Values plotted are for all the grid points where the change in NO_X mixing ratio was greater than 10 ppt. The plot symbols used reflect the CO mixing ratio for the grid points.

5.2. WINTERTIME CONDITIONS

In February the decreases in the global inventories are 0.047 Tg and 1.7 Tg for NO_X and ozone respectively, a ratio of 11 ozone molecules per NO_X. This gives a NO_Y lifetime of 6.6 days. Even though the NO_X lifetime has increased by a factor of 20 compared with the August conditions, the ozone production efficiency has decreased by a factor of about 16. So the effectiveness of the NO_X control in reducing ozone has not changed when the ozone change over the whole globe is included.

Instead of the main loss rate for NO_X being through the reaction with OH as before, it is now through the reactions NO + $O_3 \rightarrow NO_2$ and NO_2 + $O_3 \rightarrow NO_3$, $NO_3 + NO_2 \rightarrow N_2O_5$, $N_2O_5 + H_2O \rightarrow 2HNO_3$. In the summer the ozone production efficiency decreased with increasing NO_X since the increased loss of NO_X through reaction with OH reduced the NO_X lifetime, in the winter the production efficiency decreases since the NO_2 + O_3 reaction directly removes ozone and, hence, the efficiency can become negative. So in regions of high NO_X and low OH, reducing NO emissions will actually increase the ozone concentrations as there will be less titration of ozone with NO_X. This can be seen in Figure 8c which is a surface map of the percentage decrease in ozone after the emission controls. Over northern Europe the values are negative i.e. there is an increase in the ozone concentration, however over North Africa, and the eastern Mediterranean ozone levels are decreased. We do include the N_2O_5 loss with water vapour $N_2O_5 + H_2O(g) \rightarrow HNO_3$ but not the reaction with liquid water on aerosols which might affect the titration effect. Dentener and Crutzen (1993) predict upto a 25% decrease in Northern Hemisphere winter surface ozone concentrations by including the heterogeneous N_2O_5 loss and our homogeneous reaction should have a roughly similar effect. Reducing the NO_X emissions increases the near-surface ozone concentrations by over 40% in the most polluted areas. South of the polluted regions, the NO_X emission reduction again, as in summertime, leads to a reduction in ozone production. The vertical extent of the effect of the emission controls is shown in Figure 8d. Globally, the total ozone inventory decreases with NO_X emission reduction in wintertime, despite there being local ozone increases over the European continent. Liu *et al.* (1987) concluded that if nighttime nitrogen chemistry is ignored then the decrease in ozone production efficiency in the winter should be compensated for by the increase in the NO_X lifetime, so the ozone production term divided by the NO_X emission rate should be independent of season. They postulate that this will not be the case if nighttime nitrogen chemistry is important, and our results confirm that nighttime chemistry is important in the European winter.

Looking at the $d[O_3]/d[NO_X]$ ratios again in Figures 9c and d; over Europe and the Arctic the ratio is between 0 and -2 which agrees with the NO_X-ozone titration principle. Away from the pollution sources and higher in the atmosphere the ratio is positive with values up to more than 20.

Graphs of the ozone production efficiency (Figures 10c and d) show that the efficiency is mostly negative for NO_X mixing ratios greater than 1 ppb. For those efficiencies that are negative there seems to be a positive dependence on the NO_X mixing ratio. The influence of CO is less easy to determine than for the summer as the range of CO mixing ratios is only a factor of 3, there may be more reactive hydrocarbons that have a greater influence. The largest negative efficiencies occur at low OH mixing ratio which suggests that lack of OH is a cause of the ozone destruction in the winter.

6. Conclusions

A three dimensional Lagrangian model of tropospheric chemistry has been constructed which is driven by emissions, stratospheric concentrations of ozone and other species, and meteorological information. Meteorological fields used were archived from the UK Meteorological Office Unified Model. The model contains a comprehensive description of the gas phase chemistry of around fifty species, and is designed to provide an adequate description of tropospheric ozone and odd hydrogen chemistry. All the model species are integrated in the three-dimensional space, and the diurnal cycle is followed. The actinic fluxes required to define the photolysis rates are calculated by using cloud amount data archived at a frequency of four times each day. Other meteorological data used by the model include wind data to determine the three-dimensional trajectories of the Lagrangian cells, temperature to determine the thermal rate coefficients, and humidity as a catalyst in HO_2 recombination and a reactant with $O(^1D)$, an important source of free radicals. The profiles of temperature and wind are used to define the boundary layer depth, which in turn, determines whether a particular Lagrangian cell may receive emissions from the surface. The chemical scheme includes a flux algorithm which calculates the amount of material processed by each reaction.

The emissions of NO_X, carbon monoxide, methane, sulphur dioxide, hydrogen, two species of aldehydes and seven hydrocarbons are described from industrial, nonindustrial, continental, and oceanic sources. The great range of emission rates over the globe produces large concentration gradients for short-lived compounds such as NO_X which would not be obtained with a longitudinally averaged two-dimensional model. We have included the chemistry of the major hydrocarbons, which is essential for calculating features of the radical chemistry such as the $OH \leftrightarrow HO_2$ interconversion rate. As reactions of NO with free radicals dominate the photochemical production of ozone, and the reactions of ozone with OH and HO_2 are important destruction processes, it is concluded that the non-methane hydrocarbons are essential elements of any global tropospheric ozone model.

It is very important to verify model results by a careful evaluation with real data as a model is useless unless it is a good approximation to reality. The concentrations of ozone and NO_X have been compared with the available observations, and the OH concentration compared to evaluations from methyl chloroform measurement

(Prinn *et al.*, 1995). The model simulates these concentrations well, and there is particularly good agreement over regions where the surface emissions do not vary significantly over a $5^\circ \times 5^\circ$ grid square. NO_X concentrations agree with measurements very well throughout the troposphere and over both seasons suggesting that our oxidation of NO_X and removal of the products is modelled well. We overpredict ozone over rural areas close to urban centres, partly because our emission and output grids are too coarse to differentiate between rural and urban conditions, partly because we may be overpredicting ozone production. The overproduction could be caused by smearing out localised strong emission sources over a wide area or by insufficient detail in our treatment of isoprene chemistry. Another factor could be too strong convection over the continents bringing down ozone from near the tropopause. All these processes will need to be investigated further in our model. Increasing the number of Lagrangian cells in the model will improve the resolution and allow us to test the model more rigorously over industrial countries.

To understand the importance of individual reactions on a global scale, the globally accumulated production and loss terms for ozone and NO_Y have been calculated. In August, the net photochemical production of ozone was calculated to be 5.7×10^{34} molecules per day, compared with a stratospheric input at 100 mb of 8×10^{33} molecules per day.

As a first step to investigating possible ozone control strategies, the model was used to simulate the changes in ozone resulting from a 50% reduction in European NO_X emissions. The results from this experiment showed a reduction in ozone over Europe by around 10–20% in the summer, but the NO_X emission reduction was shown to have the opposite effect in the winter, increasing the ozone in the same area by over 40%. These sensitivity studies to NO_X emissions provide an interesting test of the model ozone production chemistry. In particular, the nonlinearity of the ozone production efficiency with NO_X concentration found here agrees well with that reported in other studies.

Acknowledgements

We wish to thank Karl Kitchen, Roy Maryon, Derrick Ryall and David Thomson for help with parameterisations; David Lee (AEA Technology) for help with the emissions; Mike Jenkin and Gary Hayman (AEA Technology) for help with the chemistry; Øystein Hov (University of Bergen) and David Simpson (IVL Gothenburg) with EMEP chemistry and QSSA method. We also acknowledge AQ and GA Divisions, Department of the Environment for their help and encouragement through contracts EPG 1/3/17 and PECD 7/12/37.

References

Atkinson, R., Baulch, D. L., Cox, R. A., Hampson, R. F., Kerr, J. A., and Troe, J., 1992: Evaluated kinetic and photochemical data for atmospheric chemistry, Supplement IV, IUPAC subcommittee on gas kinetic data evaluation for atmospheric chemistry, *J. Phys. Chem. Ref. Data* **21**, 1125–1568.

Atkinson, R., 1994: Gas phase tropospheric chemistry of organic compounds, *J. Phys. Chem. Ref. Data*, Monograph **2**, 1–216.

Benkovitz, C. M., Dignon, J., Pacyna, J., Scholtz, T., Tarrason, L., Volder, E., and Graedel, T. E., 1996: *Global Inventories of Anthropogenic Emissions of SO_2 and NO_X* (in preparation).

Blake, D. R. and Rowland, F. S., 1986: World wide increase in tropospheric methane, *J. Atmos. Chem.* **4**, 43–62.

Burkholder, J. B., Talukdar, R. K., Ravishankara, A. R., and Solomon, S., 1993: Temperature dependence of the HNO_3 UV absorption spectrum, submitted to *J. Geophys. Res.*

Carroll, M. A., Ridley, B. A., Montzka, D. D., Hubler, G., Walega, J. G., Norton, R. B., Huebert, B. J., and Grahek, F. E, 1992: Measurements of nitric oxide and nitrogen dioxide during the Mauna Loa Observatory Photochemistry Experiment, *J. Geophys. Res.* **97**, 10361–10374.

Chatfield, R. B. and Delany, A. C., 1990: Convection links biomass burning to increased tropical ozone: However, models will tend to overpredict O_3, *J. Geophys. Res.* **95**, 18473–18488.

Chock, D. P. and Winkler, S. L., 1994: A comparison of advection algorithms coupled with chemistry, *Atmos. Environ.* **28**, 2659–2675.

Cicerone, R. J., 1988: How has the atmospheric concentration of CO changed? in: F. S. Rowland and I. S. A. Isaksen (ed), *The Changing Atmosphere*, Wiley, New York, pp. 44–61.

Combrink, J., Diab, R. D., Sokolic, F., and Brunke, E. G., 1995: Relationship between surface, free tropospheric and total column ozone in two contrasting areas in South Africa, *Atmos. Environ.* **29**, 685–691.

Crutzen, P. J., 1974: Photochemical reactions initiated by and influencing ozone in the unpolluted troposphere, *Tellus* **26**, 47–57.

Crutzen, P. J. and Gidel, L. T., 1983: A two-dimensional photochemical model of the atmosphere, 2: The tropospheric budgets of the anthropogenic chlorocarbons, CO, CH_4, CH_3Cl and the effect of various NO_X sources on tropospheric ozone, *J. Geophys. Res.* **88**, 6641–6661.

Cullen, M. J. P., 1993: The unified forecast/climate model, *Meteorological Magazine* **122**, 81–94.

Dabdub, D. and Seinfeld, J. H., 1994: Numerical advective schemes used in air quality models – sequential and parallel implementation, *Atmos. Environ.* **28**, 3369–3385.

Dentener, F. J. and Crutzen, P. J., 1993: Reaction of N_2O_5 on tropospheric aerosols: Impact on the global distributions of NO_X, O_3, and OH, *J. Geophys. Res.* **98**, 7149–7163.

Derwent, R. G., Simmonds, P. G., and Collins, W. J., 1994: Ozone and carbon monoxide measurements at a remote maritime location, Mace Head, Ireland, from 1990 to 1992, *Atmos. Environ.* **28**, 2623–2637.

Dignon, J. and Hameed, S., 1989: Global emissions of nitrogen and sulfur oxides from 1860 to 1980, *J. Air Pollut. Control Ass.* **39**, 180–186.

Ehhalt, D. H. and Drummond, J. W., 1988: NO_X sources and the tropospheric distribution of NO_X during STRATOZ III, in: I. S. A. Isaksen (ed.), *Tropospheric Ozone*, D. Reidel, Dordrecht, pp. 217–237.

Ehhalt, D. H., Rohrer, F., and Wahner, A., 1992: Sources and distribution of NO_x in the upper troposphere at northern mid-latitudes, *J. Geophys. Res.* **97**, 3725–3738.

Eliassen, A., Hov, O., Isaksen, I. S. A., Saltbones, J., and Stordal, F., 1982: A Lagrangian long range transport model with atmospheric boundary layer chemistry, *J. Appl. Meteor.* **21**, 1645–1661.

Franzblau, E. and Popp, C. J., 1989, Nitrogen oxides produced from lightning, *J. Geophys. Res.* **94**, 11089–11104.

Gregory, G. L., Browell, E. V., and Warren, L. S., 1988: Boundary layer ozone: An airborne survey above the Amazon Basin, *J. Geophys. Res.* **93**, 1452–1468.

Guenter, A., Hewitt, C. N., Erickson, D., Fall, R., Geron, C., Graedel, T., Harley, P., Klinger, L., Lerdau, M., McKay, W. A., Pierce, T., Scholes, R., Steinbrecher, R., Tallamraju, R., Taylor, J., and Zimmerman, P., 1995: A global model of natural volatile organic compound emissions, *J. Geophys. Res.* **100**, 8873–8892.

Haagen-Smit, A. J., Bradley, C. E., and Fox, M. M., 1953: Ozone formation in photochemical oxidation of organic substances, *Ind. Eng. Chem.* **45**, 2086–2089.

Hjellbrekke, A.-G., Schaug, J., and Skjelmoen, J. E., 1996: EMEP Data Report 1994. Part 1: Annual summaries, *EMEP/CCC-Report 4/96*, NILU, Norway.

Hough, A. M., 1988: The calculation of photolysis rates for use in global tropospheric modelling studies, *AERE Report R-13259*, HMSO, London.
Hough, A. M., 1991: Development of a two-dimensional global tropospheric model: Model chemistry, *J. Geophys. Res.* **96**, 7325–7362.
Hough, A. M. and Derwent, R. G., 1990: Changes in the global concentration of tropospheric ozone due to human activities, *Nature* **344**, 645–660.
Hough, A. M. and Woods, K. J., 1988: Ozone concentrations in the global atmosphere. Analysis of data from the SBUV instrumentation the Nimbus-7 satellite, *AERE Report R-13271*, HMSO, London.
IPCC, 1995: *Climate Change 1994. Radiative Forcing of Climate Change*, Intergovernmental Panel on Climate Change, CUP, Cambridge.
Jacob, D. J. and Wofsy, S. C., 1988: Photochemistry of biogenic emissions over the Amazon forest, *J. Geophys. Res.* **93**, 1477–1486.
Jacob, D. J., Logan, J. A., Yevich, R. M., Gardner, G. M., Spivakovsky, C. M., Wofsy, S. C., Munger, J. W., Sillman, S., Prather, M. J., Rodgers, M. O., Westberg, H., and Zimmerman, P. R., 1993: Simulation of summertime ozone over North America, *J. Geophys. Res.* **98**, 14797–14816.
Kanakidou, M. and Crutzen, P. J., 1993: Scale problems in global tropospheric chemistry modeling: Comparison of results obtained with a three-dimensional model, adopting longitudinally uniform and varying emissions of NO_X and NHMC, *Chemosphere* **26**, 787–801.
Kasibhatla, P. S., Levy, H., Moxim, W. J., and Chameides, W. L., 1993: The relative impact of stratospheric photochemical production on tropospheric NO_Y levels: A model study, *J. Geophys. Res.* **96**, 18631–18636.
Komhyr, W. D., Oltmans, S. J., Franchois, P. R., Evans, W. F. J., and Matthews, W. A., 1989: The latitudinal distribution of ozone to 35 km altitude from ECC ozonesonde observations, 1985–1987, in: R. D. Bojkov and P. Fabian (eds), *Ozone in the Atmosphere*, A. Deepak, Hampton, Va, pp. 147–150.
Leighton, P. A., 1961: *Photochemistry of Air Pollution*, Academic Press, New York.
Lelieveld, J. and Crutzen, P. J., 1994: Role of deep cloud convection in the ozone budget of the troposphere, *Science* **264**, 1759–1761.
Levy, H., 1971: Normal atmosphere: Large radical and formaldehyde concentrations predicted, *Science* **173**, 141–143.
Lin, X., Trainer, M., and Liu, S. C., 1988: On the nonlinearity of the tropospheric ozone production, *J. Geophys. Res.* **93**, 15879–15888.
Liu, S. C., Trainer, M., Fehensfeld, F. C., Parrish, D. D., Williams, E. J., Fahey, D. W., Hübler, G., and Murphy, P. C., 1987: Ozone production in the rural troposphere and the implications for regional and global ozone distributions, *J. Geophys. Res.* **92**, 4191–4207.
Logan, J. A., 1983: Nitrogen oxides in the troposphere: Global and regional budgets, *J. Geophys. Res.* **88**, 10785–10807.
Logan, J. A., 1985: Tropospheric ozone, seasonal behaviour, trends and anthropogenic influence, *J. Geophys. Res.* **90**, 10463–10482.
Martinez, R. D., Buitrago, A. A., Howell, N. W., Hearn, C. H. G., and Joens, J. A., 1992: The near UV absorption spectra of several aliphatic aldehydes and ketones at 300K, *Atmos. Environ.* **26A**, 185–792.
Maryon, R. H. and Best, M. J., 1992: 'NAME', 'ATMES' and the boundary layer problem, *Met O (APR) Turbulence and Diffusion Note*, No. 204.
McKeen, S. A., Hsie, E.-Y., and Liu, S. C., 1991, A study of the dependence of rural ozone on ozone precursors in the eastern United States, *J. Geophys. Res.* **196**, 15377–15394.
Munger, J. W., Wofsy, S. C., Bakwin, P. S., Fan, S.-M., Goulden, M. L., Daube, B. C., and Goldstein, A. H., 1996: Atmospheric deposition of reactive nitrogen oxides and ozone in a temperate deciduous forest and a subarctic woodland. 1. Measurements and mechanisms, *J. Geophys. Res.* **101**, 12639–12657.
Murphy, D. M. and Fahey, D. W., 1994: An estimate of the flux of stratospheric reactive nitrogen and ozone into the troposphere, *J. Geophys. Res.* **99**, 5325–5332.
NASA Panel for Data Evaluation, 1992: *Chemical Kinetics Data for Use in Stratospheric Modeling*, Evaluation Number **9**, JPL Publications 92-20.

Nicovitch, J. M. and Wine, P. H., 1988: Temperature-dependent absorption cross-sections for hydrogen peroxide vapour, *J. Geophys. Res.* **93**, 2417–2421.
Olson, J. and Watts, J., 1982: *Map of Major World Ecosystem Complexes*, Environmental Sciences Division, Oak Ridge Nat. Lab., Tenn.
Olszyna, K. J., Bailey, E. M., Simoniatis, R., and Meagher, J. F., 1994: O_3 and NO_Y relationships at a rural site, *J. Geophys. Res.* **99**, 14557–14563.
Oltmans, S. J. and Levy, H. II, 1994: Surface ozone measurements from a global network, *Atmos. Environ.* **28**, 9–24.
Penner, J. E., Atherton, C. S., Dignon, J., Ghan, S. J., Walton, J. J., and Hameed, S., 1991: Tropospheric nitrogen: A three-dimensional study of sources, distributions and deposition, *J. Geophys. Res.* **96**, 959–990.
Poulida, O., Dickerson, R. R., Doddridge, B. G., Holland, J. Z., Wardel, R. G., and Watkins, J. G., 1991: Trace gas concentrations and meteorology in rural Virginia 1. Ozone and carbon monoxide, *J. Geophys. Res.* **96**, 22461–22475.
Price, C. and Rind, D., 1992: A simple lighting parameterization for calculating global lightning distributions, *J. Geophys. Res.* **97**, 9919–9933.
Prinn, R. G., Weiss, R. F., Miller, B. R., Huang, J., Alyea, F. N., Cunnold, D. M., Fraser, P. B., Hartley, D. E., and Simmonds, P. G., 1995: Atmospheric trends and lifetime of trichloroethane and global average hydroxyl radical concentrations based on 1978–1994 ALE/GAGE measurements, *Science* **269**, 187–192.
Rasmussen, R. A. and Khalil, M. A. K., 1986: 4. Atmospheric methane in the real and ancient atmospheres: concentrations and interhemispheric gradient, *J. Geophys. Res.* **89**, 11599–11605.
Rattigan, O., Lutman, E., Jones, R. L., Cox, R. A., Clemitshaw, K., and Williams, J., 1992: Temperature-dependent absorption cross sections of gaseous nitric acid and methyl nitrate, *J. Photochem. Photobiol. A: Chem.* **66**, 313–326.
Schumann, U., 1995: The impact of NO_X emissions from aircraft upon the atmosphere at flight altitudes 8–15 km (AERONOX), *CEC Report*, Brussels, Belgium.
Sillman, S., Logan, J. A., and Wofsy, S. C., 1990: A regional scale model for ozone in the United States with sub-grid representation of urban power plant plumes, *J. Geophys. Res.* **95**, 5731–5748.
Simpson, D., 1991: Long period modelling of photochemical oxidants in Europe, *EMEP MSC-W Note 1/91*, The Norwegian Meteorological Institute, Oslo.
Simpson, D., 1992a: Long period modelling of photochemical oxidants in Europe, *EMEP MSC-W Note 1/92*, The Norwegian Meteorological Institute, Oslo.
Simpson, D., 1992b: Long-period modelling of photochemical oxidants in Europe. Model calculations for July 1985, *Atmos. Environ.* **26A**, 1609–1634.
Simpson, D., 1993: Photochemical model calculations over Europe for two extended summer periods: 1985 and 1989. Model results and comparison with observations, *Atmos. Environ.* **27A**, 921–943.
Spiro, P. A., Jacob, D. J., and Logan, J. A., 1992: Global inventory of sulfur emissions with $1^\circ \times 1^\circ$ resolution, *J. Geophys. Res.* **97**, 6023–6036.
Stevenson, D. S., Johnson, C. E., Collins, W. J., and Derwent, R. G., 1997a: Changes to tropospheric oxidants from aircraft nitrogen oxide emissions studied with a 3-D Lagrangian model, *Atmos. Environ.* (in press).
Stevenson, D. S., Johnson, C. E., Collins, W. J., and Derwent, R. G., 1997b: Intercomparison and evaluation of atmospheric transport in a Lagrangian model (STOCHEM), and a Eulerian model (UM), using ^{222}Rn as a short-lived tracer, submitted to the *Q. J. Royal Meteorol. Soc.*
Strand, A. and Hov, O., 1994: A two-dimensional global study of tropospheric ozone production, *J. Geophys. Res.* **99**, 22877–22895.
Thomson, D. J., 1987: Criteria for the selection of stochastic models of particle trajectories in turbulent flows, *J. Fluid. Mech.* **180**, 529–556.
Trainer, M., Parrish, D. D., Buhr, M. P., Norton, R. B., Fehsenfeld, F. C., Anlauf, K. G., Bottenheim, J. W., Tang, Y. Z., Wiebe, H. A., Roberts, J. M., Tanner, R. L., Newman, L., Bowersox, V. C., Meagher, J. F., Olszyna, K. J., Rodgers, M. O., Wang, T., Berresheim, H., Demerjian, K. L., and Roychowdhury, U. K., 1993: Correlation of ozone with NO_Y in photochemically aged air, *J. Geophys. Res.* **98**, 2917–2925.
US Standard Atmosphere, 1976: US Government Printing Office, Washington DC.

Turman, B. N. and Edgar, B. C., 1982: Global lightning distributions at dawn and dusk, *J. Geophys. Res.* **87**, 1191–1206.
Volz, A. and Kley, D., 1988: Evaluation of the Montsouris series of ozone measurements made in the nineteenth century, *Nature* **332**, 240–242.
Walton, J., MacCracken, M., Ghan, S., 1988: A global-scale Lagrangian trace species model of transport, transformation, and removal processes, *J. Geophys. Res.* **93**, 8339–8354.
Warneck, P., 1988: *Chemistry of the Natural Atmosphere*, Academic Press, San Diego, California, pp. 158–170.
Winkler, P., 1988: Surface ozone over the Atlantic Ocean, *J. Atmos. Chem.* **7**, 73–91.
WHO, 1987: *Air Quality Guidelines for Europe*, WHO Regional Publications, European series No. **23**, Word Health Organization, Copenhagen, Denmark.
WMO, 1986: Atmospheric Ozone 1985, assessment of our understanding of the processes controlling its present distribution and change, *Global Ozone Research and Monitoring Project*, Report No. 16, World Meteorological Organisation, Geneva.
WMO, 1995: Scientific assessment of ozone depletion: 1994, *World Meteorological Organisation. Global Ozone Research and Monitoring Project*, Report No. 37, Geneva.
Yienger, J. J. and Levy, H. III, 1995: An empirical model of global soil-biogenic NO_X emission, *J. Geophys. Res.* **100**, 11447–11464.